Aerospace Science and Technology 158 (2025) 109949

Contents lists available at ScienceDirect

Aerospace Science and Technology

journal homepage: www.elsevier.com/locate/aescte

Optimal planning and tracking for E-sail transition between steady-states

Guillermo Pacheco-Ramos [a,*], Rafael Vazquez [a], Daniel Garcia-Vallejo [b]

[a] Department of Aerospace Engineering, Universidad de Sevilla, Seville, Spain
[b] Department of Mechanical Engineering and Manufacturing, Universidad de Sevilla, Seville, Spain

ARTICLE INFO

Communicated by Damiano Casalino

Keywords:
Electric solar wind sail
E-sail
Optimal planning
Model predictive control
Trajectory tracking
Optimal control

ABSTRACT

The E-sail technology employs the repulsive force of solar wind protons on positively charged tethers for continuous propulsion. Mission research highlights the necessity to modulate thrust, while dynamics studies reveal a tendency for oscillation. This study explores achieving stable transitions between different E-sail steady-states, each associated to varying voltages and thrust levels. By creating a simplified multibody model with straight, rigid tethers, controlled transitions are investigated, considering the system's underactuated nature. An optimal control perspective is adopted to minimize a cost function for optimal planning. Additionally, the system's response to open-loop control actions is examined, underscoring the need for feedback to ensure precise trajectory tracking. Consequently, a procedure for deriving a feedback control law using Model Predictive Control is proposed. The results suggest the feasibility of stable transitions using underactuated control and advocate for applying these methods to more complex and realistic scenarios.

1. Introduction

The E-sail is a propulsion technology, proposed by Janhunen [1], that generates thrust without using propellant by harnessing the momentum of solar wind protons as described in Fig. 1(a). The E-sail is included within the group of propellantless and continuous-thrust propulsion systems, which, while in some scenarios may entail longer transfer times, are of great interest for transfers requiring high energy or very long duration. The applications summarized by Janhunen [2] and further reviewed by Bassetto [3], demonstrate the E-sail's capabilities as a propulsion system, while various works underscore the importance of modulating thrust throughout the mission and even turning the system on or off as needed [4,5].

The most common architecture of E-sails comprises a set of tethers arranged radially around the main spacecraft [3], represented in Fig. 1(b). These tethers, which are electrical conductors, are maintained at a high electrical potential thanks to an electron gun system. The rotation of the assembly allows for the stiffening and stabilization of the tethers, facilitated by the presence of remote units positioned at the outer end of each tether. However, several factors that can disrupt the angular velocities of the different tethers have been identified in various works. These factors include the emergence of transverse propulsive forces when operating in configurations where the axis of rotation is not parallel to the solar rays (non-null sailing angle) [6], Coriolis forces [7], solar wind fluctuations [8], and the system's own dynamics when studied from a multibody perspective [9]. To address these challenges, various enhancements to the basic E-sail configuration have been proposed. One such enhancement involves the incorporation of small thrusters into the aforementioned remote units [10], allowing for independent regulation of each tether's angular velocity. Additionally, the connection of remote units via auxiliary tethers has been considered and demonstrated to stabilize the system [10,11]. In relation to auxiliary or secondary tethers, as they are also called, there are different configurations, some studies propose the use of conductive auxiliary tethers, which allow for an additional control parameter to regulate the angular velocity of the assembly [8]. Under the consideration of simplified dynamics, it is demonstrated that using an appropriate modulation strategy makes it possible to control the propulsive force, the attitude of the E-sail, as well as the oscillations of the tethers and the angular velocity. Alternative configurations include the use of photonic blades, similar to the heliogyro [12,13], which can also aid in controlling the angular velocities of each tether and achieving modification of the spin rate of the assembly [14,15].

* Corresponding author.
E-mail addresses: gpacheco@us.es (G. Pacheco-Ramos), rvazquez1@us.es (R. Vazquez), dgvallejo@us.es (D. Garcia-Vallejo).

https://doi.org/10.1016/j.ast.2025.109949
Received 10 November 2024; Received in revised form 27 December 2024; Accepted 8 January 2025

Available online 10 January 2025

Nomenclature

Roman symbols

A	Cross-sectional area.
$\mathbf{c}$	Constrains vector of OCP.
$\mathbf{c}_b$	Constrains associated to initial boundary conditions.
$\mathbf{c}_d$	Constrains associated to dynamic equations.
$\mathscr{E}$	Mayer term of the cost function.
F	Thrust force magnitude.
$\mathbf{f}$	Generalized force vector of the first-order system.
$\mathbf{f}'$	Generalized force vector of the second-order system.
$\mathbf{f}_c$	Generalized Coulomb force vector per unit of length.
f_V	Coulomb force magnitude.
f_w	Equivalent solar wind factor.
h	Time discretization step.
h_r	Height of the central vehicle.
H_c	Duration of the control horizon.
H_o	Total duration of the transition maneuver.
H_p	Duration of the prediction horizon.
j	Inertia respect to the spin axis.
$\mathscr{J}$	Cost function for optimization problem.
$\boldsymbol{J}$	Inertia respect to the anchor point.
$\mathscr{L}$	Lagrange term of the cost function.
L	Body Length.
m	Body mass.
$\mathbf{M}'$	Mass matrix of the second-order system.
$\mathbf{M}$	Mass matrix of the first-order system.
M_c	Central vehicle control moment around X_B axis.
m_w	Solar wind proton mass.
n	Number of generalized coordinates of the system.
N_c	Control horizon.
N_o	Number of successive OCPs to be solve for tracking.
N_p	Prediction horizon.
n_w	Solar wind plasma density.
p	Number of tethers.
$p_\oplus$	Solar wind dynamic pressure.
$\mathbf{Q}$	Generalized force.
$\mathbf{q}$	Generalized coordinates vector.
r	Position of the central vehicle along X_H axis.
R_r	Radius of the central vehicle.
T	Kinetic energy.
t	Time.
t_f	Final time for E-sail transition.
t_i	Initial time for E-sail transition.
t_m	Duration of transition between steady-states.
T_s	Spin period.
$\mathbf{u}$	Control vector.
u_w	Bulk solar wind velocity.
V_+	Voltage corresponding to the bulk kinetic energy of a solar wind proton.
V_j	Voltage value for j-th tether.
$\mathbf{x}$	State vector.

Greek symbols

β_j	Lagging angle of the j-th tether.
δx	Virtual variable x.
ϵ_0	Vacuum permittivity.
ϵ_c	Acceptable control error for angular position.
$\dot{\epsilon}_c$	Acceptable control error for angular velocity.
ϵ_p	Acceptable planning error for angular position.
$\dot{\epsilon}_p$	Acceptable planning error for angular velocity.
γ_j	Coning angle of the j-th tether.
$\boldsymbol{\Lambda}$	Weight matrix for states.
ϕ	Angular position of the central vehicle Y_B axis respect to Y_R axis.
ρ	Body mass density.
$\boldsymbol{\Sigma}$	Weight matrix for controls.
ζ_j	Angular position for the j-th tether anchor point with respect to Y_B axis.

Superscripts

$*$	State or control associated to optimal tracking solution.
0	State or control associated to initial iterant for OCP.
$\perp$	Solar wind velocity component perpendicular to the tether.
p	State or control associated to optimal planning.
r	State or control associated to reference.
t	State associated to system trajectory computed by time integration considering actual solar wind evolution.

Subscripts

0	Reference/nominal value of magnitude.
B	Expressed in the body coordinate system B.
e	Property associated to the E-sail system.
G_j	Expressed in the j-th auxiliary coordinate system G_j.
H	Expressed in heliocentric inertial coordinate system.
N_j	Expressed in the j-th auxiliary coordinate system N_j.
R	Expressed in the reference coordinate system R.
r	Property associated to central vehicle.
s	State or control associated to steady-state.
t	Property associated to tether.
u	Property associated to remote unit.
w_0	Solar wind average conditions at 1 AU.
Z_j	Expressed in the j-th tether local coordinate system Z_j.

Other symbols

$\dot{x}$	First time derivative.
$\ddot{x}$	Second time derivative.
$\hat{x}$	Normalized error of the magnitudes with respect to the reference.
$\overline{x}$	Normalized magnitude.
$\oslash$	Hadamard division

Acronyms

ANCF	Absolute Nodal Coordinate Formulation.
CME	Coronal Mass Ejection.
DAE	Differential Algebraic Equation.
EDT	Electrodynamics Tethers.
E-sail	Electric solar wind sail.
EUPHORIA	European Prediction Of Heliospheric Indices and Cosmic Rays.
MPC	Model Predictive Control.
NLP	Nonlinear Programming.
NPFEM	Nodal Position Finite Element Method.
OCP	Optimal Control Problem.
ODE	Ordinary Differential Equation.
SHMPC	Shrinking Horizon Model Predictive Control.
TSS	Tethered Satellite System.

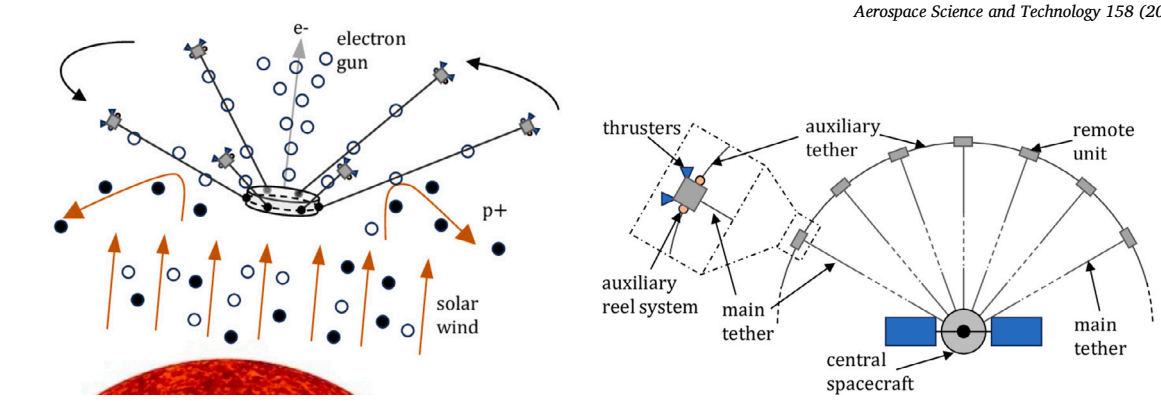

(a) Conceptual scheme. (b) Main components of typical architecture.

Fig. 1. Description of Electric solar wind sail (E-sail) propulsion system.

In regards to the E-sail dynamics, early research on E-sail dynamics proposed using a spherical pendulum model [6] to model tethers as rotating rigid thin wires affected by orbital and Coulomb forces, ensuring stable evolution and control via tether voltage modulation. This model was later improved to include centrifugal forces from the E-sail's spin [16], establishing criteria for spin frequency selection and voltage modulation on secondary tethers to compensate for orbit Coriolis forces, enhancing the propellantless nature of the E-sail. Further refinements include deriving control efficiency using a single rotating tether model [17] and developing analytical approximations, valid for steady-state operation, which consider realistic sail shapes under Coulomb and centrifugal forces [18–21]. Numerical approaches, such as lumped mass models [8,22] and the Nodal Position Finite Element Method (NPFEM) [23–25], have also been used to explore the E-sail dynamics, including the influence of spin rate and the necessity of remote units to control spin rate [26,27]. Additionally, the Absolute Nodal Coordinate Formulation (ANCF) [9,28,29] and other methods have been investigated for defining control strategies for flexible E-sails [30].

Regarding control applications in E-sails, proportional controllers have been proposed in [6,8,25] to achieve attitude changes by adjusting the tether voltages. The regulation of angular velocity using proportional feedback control to modulate the control torque applied to the central vehicle and the forces on remote units is studied in [26]. In [31], Lyapunov stability functions are used to establish a control law that ensures stable deployment while in [32] is considered for E-sail attitude control and stability. More advanced methods, such as Model Predictive Control (MPC), have also been explored in the context of electric solar sails for trajectory tracking in the presence of solar wind fluctuations [5] and for E-sail coupled orbital-attitude control [33]. MPC has also been considered to reduce tether oscillations [34] and for maneuver execution [35–37]. Additionally, in the context of Tethered Satellite Systems (TSS), MPC application to tether deployment has also been explored [38,39] and in the field of Electrodynamics Tethers (EDT), particularly for deorbit control [40]. The applications of MPC in the space domain are extensive and diverse, ranging from rendezvous operations to the flight of formation constellations. A fairly rigorous compilation of these can be found in [41], and can be complemented in the realm of rendezvous and docking [42–45], attitude control [46–49], or planning and trajectories [50].

In light of the preceding discussion, the relevance of the E-sail as a propulsion system is evident, as is the necessity of adjusting thrust levels to ensure controlled and bounded dynamics. Moreover, the emphasis on simplifying the system architecture to reduce mass and deployment complexity further justifies the removal of auxiliary tethers. The significance of employing a multibody dynamic model that accounts for tether flexibility has also been underscored. Additionally, the increasing application of MPC techniques in space systems and TSS validates their consideration in this context.

Building on these insights, this work explores the feasibility of achieving stable transitions between steady states in an E-sail system with varying voltages and thrust levels. For this initial investigation, a simplified scenario is adopted, involving an analytical multibody model expressed in Ordinary Differential Equation (ODE) form, considering straight, rigid tethers and assuming rectilinear motion and fixed attitude of the central vehicle. By considering voltage modulation and control moment application on the central vehicle using a reaction wheel as control actions, the resulting system is underactuated. Given this model, the problem of inverting the dynamics to determine the control actions that enable a stable transition between initial and target steady-states is addressed. The control problem is formulated as the minimization of a cost function subject to nonlinear constraints, solved using a direct transcription method, which yields optimal transition planning through a reference trajectory and an optimal control law. Additionally, the system's response to the application of the open-loop optimal control law is studied, focusing on the need for feedback to mitigate deviations from the reference trajectory in the presence of solar wind fluctuations and initial position errors in the tethers relative to the steady-state configuration. Consistent with the planning phase, the tracking problem is approached from a MPC perspective. By adopting a Shrinking Horizon MPC (SHMPC) approach, successive optimal control problems are posed and solved, providing a feedback control law that improves the tracking of the planned trajectory. To validate the robustness of this approach under realistic conditions, a Monte Carlo analysis is performed.

The main contributions of this work are as follows: (1) investigating the feasibility of achieving controlled transitions for an E-sail without secondary tethers, using underactuated control within a multibody framework, and considering non-homogeneous initial tether position deviations and realistic solar wind fluctuations; (2) proposing an optimal approach for E-sail maneuver planning and tracking, which, due to its versatility and adaptability, can be applied to more complex systems, including those represented in Differential Algebraic Equation (DAE) form; and (3) analyzing the impact of transition time and thrust increment on control demands, providing valuable insights for system design.

The present article is organized as follows. Following the introduction, Sect. 2 describes the formulation of the multibody E-sail model, including the definition of the coordinate systems and the Lagrangian dynamics formulation. Next, Sect. 3 presents the formulation of the transition problem, where the steady-state operation is defined and the transition maneuver is established. Subsequently, the dynamic inversion for optimal transition planning and the feedback control approach for optimal trajectory tracking are introduced. The simulation results for both the planning and tracking phases are presented and discussed in Sect. 4. Finally, conclusions and directions for future work are outlined in Sect. 5.

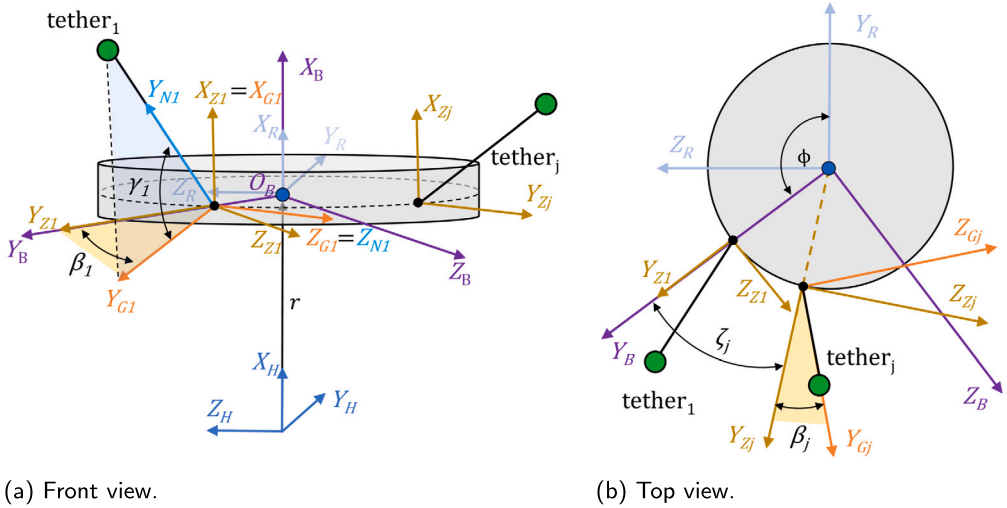

Fig. 2. Description of E-sail model coordinates.

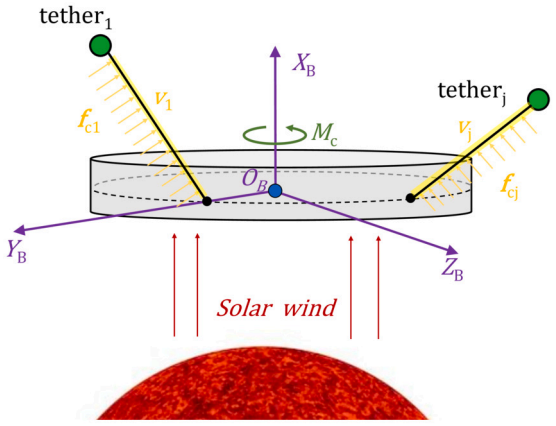

Fig. 3. Description of E-sail control forces: vector of voltage modulations $\mathbf{V}$, responsible of the generation of Coulomb forces at each tether $\mathbf{f}_{c_j}$ and control torque at central vehicle applied on spin axis M_c.

2. Simplified multi-body model formulation for an E-sail

In this section, the formulation of a simplified multi-body model for an electric solar wind sail (E-sail) is presented. The objective of this model is to facilitate a more straightforward analysis of its dynamic characteristics and to reduce the computational costs associated with its usage. In line with the conclusion drawn in [24], gravitational forces, being long-term effects, are neglected in the formulation. Consequently, this work focuses exclusively on the E-sail's attitude dynamics and does not consider its orbital mechanics.

The Lagrangian formulation is employed to define this analytical model described in Fig. 2(a) and (b), which includes the main vehicle, radial cables or tethers, and remote units located at the far end of the cables. In regards to the central vehicle, it is considered to be cylindrical, with height h_r and radius R_r, and defined by its mass m_r and moment of inertia I_r. It's worth noting that its geometric center is the origin of the body reference system B. The E-sail is considered to incorporate p tethers, which are assumed to be straight and rigid with a length L_t, cross section A_t, mass density ρ_t, corresponding to tether mass m_t and moment of inertia about their ends denoted as J_t. The remote units are considered as point masses with a value of m_u located at the further end of each tether. Additionally, the origin of the body axis system B, is situated along the X_H axis of the heliocentric inertial system H. Thus, a rectilinear motion of the central vehicle's geometric center is assumed, and its position is defined by its distance from the Sun denoted as r. Moreover, it is established that the axis of symmetry X_B is aligned with the X_H axis, such that the solar rays are parallel to the sail's spin axis. This configuration is known as a zero sailing angle. The orientation of the body axis system B relative to the inertial system is exclusively defined by the roll angle ϕ while the orientation of tethers is given by the vectors of coning angles $\boldsymbol{\gamma}$ and lagging angles $\boldsymbol{\beta}$. All the coordinates mentioned constitute a minimum set of coordinates $\mathbf{q} = \begin{bmatrix} r & \phi & \boldsymbol{\gamma}^\top & \boldsymbol{\beta}^\top \end{bmatrix}^\top$, used to formulate the dynamic of the system in ODE form and avoiding the appearance of additional coordinates or constraints forces in comparison to formulations in DAE form considering absolute coordinates [9,51]. In reference to the control actions, described in Fig. 3, the formulation considers the application of control by means of the voltage modulation $\mathbf{V}$, and control moment at the central vehicle M_c, leading to the control vector $\mathbf{u} = \begin{bmatrix} M_c & \mathbf{V}^\top \end{bmatrix}^\top$.

The coordinate frames used in this formulation are described in Fig. 2(a) and (b), and established as it follows. The heliocentric inertial coordinate system, denoted as H, is used as the absolute frame of reference. The reference frame R is established at the geometrical center of the central vehicle and parallel to H, and it moves with the E-sail. The orientation of the central vehicle is defined by the body coordinate system, referred to as B respect to the R frame. The body frame has its origin also positioned at the geometric center of the main body. The X_B axis aligns with the symmetry axis of the central body, following the orientation of X_R. The Y_B axis is established by the anchor point of tether 1, and Z_B completes

the right-handed coordinate system. At the anchor point of each tether j, a local frame Z_j is established and defined as it follows: the X_{Z_j} axis is parallel to X_B and the Y_{Z_j} axis aligns with the radial direction going outwards. The orientation of coordinate system Z_j respect to B is given a rotation around X_B of angle ζ_j, which is constant for each tether. A rotation of angle β_j around the X_{Z_j} allows to defined the intermediate lagging frame G_j, where the axis Z_{G_j} and Y_{G_j} lie in the $Y_B Z_B$ plane. An additional rotation of angle $-\gamma_j$ around Z_{G_j} establishes the final orientation of the tether j and its associated coning frame N_j. The sequence of transformations allowing to defined the orientation of the tether frame N_j respect to the inertial coordinate system H, can be summarized as

$$R \xrightarrow[X_R]{\phi} B \xrightarrow[X_B]{\zeta_j} Z_j \xrightarrow[X_{Z_j}]{\beta_j} G_j \xrightarrow[Z_{G_j}]{-\gamma_j} N_j. \tag{1}$$

2.1. Kinetic energy

The total kinetic energy of the system, T_e, considering the contributions of the central vehicle, T_r, the tethers T_{t_j} and the remote units T_{u_j}, for $j = 1, ..., p$, can be written as

$$T_e = T_r + \sum_{j=1}^{p} \left(T_{t_j} + T_{u_j} \right). \tag{2}$$

Where, for the sake of briefness, the detailed expression of each contribution is provided in Appendix A.

2.2. Generalized forces

The generalized forces $\mathbf{Q}$ considered for the formulation of the simplified model proposed, are introduced in this section. The propulsive force generated by Coulomb effect associated to the voltage modulation of the tethers and the application of a control torque in the central vehicle are considered. Their formulation and the assumptions considered are provided hereafter.

2.2.1. Coulomb forces

The estimation of the thrust generated on a charged wire under the influence of the solar wind, has been investigated considering different approaches and leading to definition of various thrust models for the prediction of the propulsive force [52–56]. Although the predictions of the induced forces, calculated using the previous mentioned models, lead to notable quantitative differences, it has been shown that the impact of the thrust model considered on the E-sail dynamics is negligible [27]. The approximation proposed in [57], valid for a tether exposed to the solar wind at 1AU from the Sun, is considered in the current work. Under these conditions, the magnitude of the thrust force per unit of length of the j-th tether can be estimated as:

$$f_{c_j} \approx 0.18 \max(0, V_j - V_+) \sqrt{\epsilon_0 p_\oplus} \approx 0.18 \max(0, V) \sqrt{\epsilon_0 p_\oplus}, \tag{3}$$

where V_j is the tether voltage (typically between 20-40 kV), V_+ represents the voltage corresponding to the bulk kinetic energy of a solar wind proton, typically $V_+ = 1$kV, and ϵ_0 stands for the vacuum permittivity, equal to $8.854 \times 10^{-12}\,\mathrm{F\,m^{-1}}$. Given the typical ranges exposed for V and V_+, the V_+ term can be neglected [57]. Additionally, $p_\oplus$ is the solar wind dynamic pressure defined as

$$p_\oplus = m_w\, n_w\, u_w^2, \tag{4}$$

being m_w the solar wind proton mass, n_w the solar wind plasma density and u_w the magnitude of the bulk solar wind speed. The values of solar wind magnitudes, are highly dependent of the distance from the Sun and can be approximated by simple models [58,59]. However, there are other sources of more stochastic fluctuations that can result in significant variations from the mean parameter values, as corroborated by measurements obtained by a number of space missions, such as Voyager 2 [60], Ulysses [61], and ACE [62]. The data obtained from these measurements have allowed modeling such variations using probability functions, proposing in [63] the use of the gamma function. The solar wind fluctuations have been a significant effect in different areas of E-sail studies, such as trajectory design and guidance [5,63,64]. In this work, their effect on system dynamics and the establishment of the necessary control to ensure stable system operation is of interest. Therefore, it is necessary to have not a probability function, but a time series that realistically captures the stochastic fluctuations of the solar wind. In this regard, there are different models developed by agencies or research centers, among which Enlil stands out, which was developed by NASA's Space Weather Laboratory [65], and EUPHORIA (European Prediction Of Heliospheric Indices and Cosmic Ray), funded by the European Union [66]. These three-dimensional and pseudo-empirical models use observed plasma conditions in the solar corona as well as in situ measurements of the solar wind to simulate solar wind dynamics from the solar corona to the heliosphere, allowing the prediction of solar events such as coronal mass ejections (CMEs) and geomagnetic storms to Earth and other planets in the solar system. By using these models, it is possible to obtain for a specific location within the ecliptic plane, the temporal evolution of plasma density and wind speed, which allow the calculation of dynamic pressure.

Considering the previous aspects, for this work, the Coulomb force model is established as follows:

- An E-sail operating at 1 AU from the Sun with a nominal voltage of $V_0 = 20$ kV is considered, making the Coulomb force approximation per unit length given by Eq. (3) applicable.
- The nominal solar wind is set as one characterized by the average solar wind parameters at 1 AU, thus velocity $u_{w_0} = 400$ km/s and a plasma density $n_{w_0} = 7.3\,\mathrm{cm^{-3}}$ and $m_{w_0} = 1.67 \times 10^{-27}\,\mathrm{kg}$, resulting in a nominal pressure $p_{\oplus_0}$.
- The temporal evolution of solar wind magnitudes is considered, obtained from Enlil for a given instant and positions within the ecliptic plane.
- Only the effect of u_w and n_w on the dynamic pressure $p_\oplus$ is considered, neglecting other effects such as the variation of the electron sheath radius. Thus, for conditions other than nominal, for the j, the force per unit length is written as

$$f_{c_j} = 0.18 \max(0, V_j) \sqrt{\epsilon_0\, p_\oplus} = 0.18 \max(0, V_j) \sqrt{\epsilon_0\, p_{\oplus_0}}\, f_w, \tag{5}$$

where the equivalent solar wind factor f_w is used, defined in terms of density and velocity as

$$f_w = \frac{\sqrt{n_w}\, u_w}{\sqrt{n_{w_0}}\, u_{w_0}}, \tag{6}$$

and which establishes how the dynamic pressure fluctuation modifies the generated force compared to what would be obtained with the same voltage under average solar wind conditions.

Keeping in mind that the effective force per unit of length is exclusively due to the component of the solar wind perpendicular to the tether, the resultant force vector per unit of length $\mathbf{f}_{c_j}$, expressed in N/m, can be written as [28]

$$\mathbf{f}_{c_j} = 0.18 \max(0, V) \sqrt{\epsilon_0\, m_{w_0}\, n_{w_0}}\, \mathbf{u}_{w_0}^{\perp}\, f_w, \tag{7}$$

where $\mathbf{u}_{w_0}^{\perp}$ represents the average solar wind component perpendicular to the j-th tether and which is computed based on the orientation of the tether given by ϕ, ζ_j, β_j and γ_j. The previous definitions, allows to write the virtual work associated to the Coulomb forces generated at tether j as

$$\delta W_{f c_j} = \int_0^{L_t} \mathbf{f}_{c_j}^{\top} \delta \mathbf{r}_{xj}^{I}\, \mathrm{d}x, \tag{8}$$

being the resultant expression of force vector $\mathbf{f}_{c_j}$

$$\mathbf{f}_{c_j} = f_{c_j} \begin{bmatrix} \left(1 - \sin\left(\gamma_j\right)^2\right) \\ -\cos\left(\beta_j + \phi + \zeta_j\right) \cos\left(\gamma_j\right) \sin\left(\gamma_j\right) \\ -\sin\left(\beta_j + \phi + \zeta_j\right) \cos\left(\gamma_j\right) \sin\left(\gamma_j\right) \end{bmatrix}, \tag{9}$$

where f_{c_j} is defined for each tether j as per Eq. (5).

2.2.2. Central vehicle control torque

Finally, the contribution of the control torque M_c applied to the central vehicle using a reaction wheel oriented along the primary spin axis X_B, is computed as

$$\delta W_c = M_c\, \delta\phi, \tag{10}$$

where $\delta\phi$ represents the virtual angular position of the body axis Y_B respect to Y_R as described in Fig. 2(b). It should be noted that although the use of reaction wheels to apply control torque can lead to well-known saturation issues, the study of these aspects lies beyond the scope of the present work, and only limitations associated with the actuator's magnitude range are considered.

2.3. Lagrangian dynamics

This section presents the calculation of the terms and generalized forces associated to the Lagrange's equation

$$\frac{d}{dt}\left(\frac{\partial T_e}{\partial \dot{\mathbf{q}}_j}\right) - \frac{\partial T_e}{\partial \mathbf{q}_j} - \mathbf{Q}_j = 0, \quad j = 1, \ldots, n, \tag{11}$$

where the generalized coordinates $r, \phi, \boldsymbol{\gamma}, \boldsymbol{\beta}$ are considered, and result in a set of $n = 2 + 2p$ variables, consisting of the position of the vehicle along X_H axis, its the angular position, and the vectors of angular position of the tethers, each composed of p element. The kinetic energy and generalized forces introduced in Sect. 2.1 and 2.2, respectively, allows to rewrite the Lagrange equation as the following set of dimensionless expressions in term of the independent dimensionless generalized coordinates and time derivatives. These dimensionless equations reduce the number of parameters and facilitate the identification of dominant effects. Firstly, the equation obtained for r can be written as:

$$\ddot{\overline{r}} + \frac{1}{2}\overline{m}_{t+u} \sum_{k=1}^{p} \left(\ddot{\overline{\gamma}}_k \cos\left(\gamma_k\right) - \sin\left(\gamma_k\right) \dot{\overline{\gamma}}_k^2\right) - \overline{f}_{V_0} f_w \sum_{k=1}^{p} \left(\overline{V}_k \cos^2\left(\gamma_k\right)\right) = 0, \tag{12}$$

secondly, the expression computed for ϕ is:

$$\begin{aligned} &\overline{I}_{r+t}\, \ddot{\overline{\phi}} + \sum_{k=1}^{p} \Bigg(\left(\overline{J}_{t+u} \cos^2\left(\gamma_k\right) + \frac{\overline{m}_{t+u}}{2} \cos\left(\beta_k\right) \cos\left(\gamma_k\right) \right) \left(\ddot{\overline{\phi}} + \ddot{\overline{\beta}}_k \right) - \frac{\overline{m}_{t+u}}{2} \sin\left(\beta_k\right) \sin\left(\gamma_k\right) \ddot{\overline{\gamma}}_k \\ &- \left(\frac{\overline{m}_{t+u}}{2} \cos\left(\gamma_k\right) \sin\left(\beta_k\right) \right) \left(\dot{\overline{\gamma}}_k^2 + \dot{\overline{\beta}}_k^2 + 2\dot{\overline{\phi}}\dot{\overline{\beta}}_k \right) - \left(\overline{J}_{t+u} \sin^2\left(\gamma_k\right) + \overline{m}_{t+u} \cos\left(\beta_k\right) \sin\left(\gamma_k\right) \right) \left(\dot{\overline{\phi}} + \dot{\overline{\beta}}_k \right) \dot{\overline{\gamma}}_k \\ &+ \frac{\overline{f}_{V_0} f_w}{2} \overline{V}_k \sin\left(\beta_k\right) \sin\left(2\gamma_k\right) \Bigg) - \overline{M}_c\, \overline{M}_{c_0} = 0. \end{aligned} \tag{13}$$

Thirdly, the p equations associated to the coning angle γ_j, for $j = 1, .., p$, can be written as

Table 1
Description of the main parameters considered for the definition of the E-sail baseline configuration.

Body	Dimension	Value
Main spacecraft	height, h_r [m]	2.0
	outer radius, R_r [m]	1.0
	density, ρ_r [kg/m^3]	884.0
Tethers	number of tethers, p [-]	4
	nominal length, L_t [km]	10.0
	section area, A_t [mm^2]	$4.3 \cdot 10^{-3}$
	density, ρ_t [kg/m^3]	7653.0
Remote unit	mass, m_u [kg]	1.5
E-sail	Nominal spin rate, $\dot{\phi}_0$ [rad/s]	$4.0 \cdot 10^{-3}$
	Nominal tether voltage, V_0 [kV]	20.0
	Nominal control torque, M_{c_0} [N·mm]	10.0

$$\overline{J}_{t+u}\ddot{\overline{\gamma}}_j - \frac{\overline{m}_{t+u}}{2}\sin(\beta_j)\sin(\gamma_j)\ddot{\overline{\phi}} + \frac{\overline{m}_{t+u}}{2\overline{R}_r}\cos(\gamma_j)\ddot{\overline{r}} + \frac{\overline{m}_{t+u}}{2}\cos(\beta_j)\sin(\gamma_j)\dot{\overline{\phi}}^2 + \frac{\overline{J}_{t+u}}{2}\sin(2\gamma_j)\left(\dot{\overline{\beta}}_j + \dot{\overline{\phi}}\right)^2 - \frac{\overline{f}_{V_0} f_w}{2\overline{R}}\overline{V}_j\cos(\gamma_j) = 0, \tag{14}$$

and finally, for the in plane lagging angle β_j:

$$\overline{J}_{t+u}\cos^2(\gamma_j)\left(\ddot{\overline{\beta}}_j + \ddot{\overline{\phi}}\right) + \frac{\overline{m}_{t+u}}{2}\cos(\gamma_j)\cos(\beta_j)\ddot{\overline{\phi}} + \frac{\overline{m}_{t+u}}{2}\cos(\gamma_j)\sin(\beta_j)\dot{\overline{\phi}}^2 - \overline{J}_{t+u}\sin(2\gamma_j)\left(\dot{\overline{\phi}} + \dot{\overline{\beta}}_j\right)\dot{\overline{\gamma}}_j = 0. \tag{15}$$

Where the dimensionless parameters and coordinates considered are described as follows. The normalized mass $\overline{m}_{t+u}$, is defined as $\overline{m}_{t+u} = (m_t + 2m_u)/m_e$, where the total E-sail mass is denoted as $m_e = m_r + p(m_t + m_u)$. In addition, the dimensionless overall spin inertia is expressed as $\overline{I}_{r+t} = (I_r + p\, m_t\, R_r^2)/(m_e\, L_t\, R_r)$, the normalized tether inertia respect to the anchor point is represented by $\overline{J}_{t+u} = (J_t + m_u\, L_t^2)/(m_e\, L_t\, R_r)$, and the normalized main spacecraft radius is defined as $\overline{R}_r = R_r/L_t$. Furthermore, the coordinates and their derivatives are also normalized using the dimensionless time, $\overline{t} = t/T_s$, where the spin period T_s, is given by $T_s = 2\pi/\dot{\phi}_0$, being $\dot{\phi}_0$ the nominal angular velocity of the E-sail around X_B axis, also referred to as nominal spin. The dimensionless position along X_H, $\overline{r}$, is established as $\overline{r} = r/L_t$, and its normalized acceleration with respect to $\overline{t}$ is written as $\ddot{\overline{r}} = \ddot{r}/(L_t/T_s^2)$. Similarly, the rest of the second-order time derivatives are $\ddot{\overline{\gamma}}_j = \ddot{\gamma}_j/(1/T_s^2)$, $\ddot{\overline{\beta}}_j = \ddot{\beta}_j/(1/T_s^2)$ and $\ddot{\overline{\phi}} = \ddot{\phi}/(1/T_s^2)$. Finally the corresponding velocities as $\dot{\overline{\gamma}}_j = \dot{\gamma}_j/(1/T_s)$, $\dot{\overline{\beta}}_j = \dot{\beta}_j/(1/T_s)$ and $\dot{\overline{\phi}} = \dot{\phi}/(1/T_s)$. To conclude, the controls are also normalized. The dimensionless voltage control, $\overline{V}_j$, is established as $\overline{V}_j = V_j/V_0$, being V_0 the nominal voltage modulation, and defining $\overline{f}_{V_0} = f_{V_0}/(m_e\, L_t/T_s^2)$ where $f_{V_0} = 0.18\, V_0\sqrt{\epsilon_0\, m_{w_0}\, n_{w_0}}\, u_{w_0}$ is the nominal Coulomb force magnitude and f_w the equivalent solar wind factor defined in Eq. (6). Finally, the dimensionless control torque applied at the central vehicle is similarly established by the definition of a normalized control moment $\overline{M}_c = M_c/M_{c_0}$, where M_{c_0} is the nominal control moment value, and establishing the normalized control moment as $\overline{M}_{c_0} = M_{c_0}/(m_e\, L_t\, R_r/T_s^2)$. The nominal values for the controls are provided in Table 1.

The observation of the structure of the ODE system described by Eq (12)-(15), formed by $2n+2$ equations, reveals the following insights. First, it's noted that the acceleration of the central vehicle, given by $\ddot{\overline{r}}$, is a system output as neither the state, $\overline{r}$, nor its first derivative, $\dot{\overline{r}}$, are present in the equations. By substituting Eq. (12) into Eq. (14) the obtained expression

$$\overline{J}_{t+u}\ddot{\overline{\gamma}}_j - \frac{\overline{m}_{t+u}}{2}\sin(\beta_j)\sin(\gamma_j)\ddot{\overline{\phi}} + \frac{\overline{m}_{t+u}}{2}\cos(\beta_j)\sin(\gamma_j)\dot{\overline{\phi}}^2 + \frac{\overline{J}_{t+u}}{2}\sin(2\gamma_j)\left(\dot{\overline{\beta}}_j + \dot{\overline{\phi}}\right)^2 + \frac{\overline{m}_{t+u}}{2\overline{R}_r}\cos(\gamma_j)\left(-\frac{1}{2}\overline{m}_{t+u}\sum_{k=1}^{p}\left(\ddot{\overline{\gamma}}_k\cos(\gamma_k) - \sin(\gamma_k)\dot{\overline{\gamma}}_k^2\right) + \overline{f}_{V_0} f_w\sum_{k=1}^{p}\left(\overline{V}_k\cos^2(\gamma_k)\right)\right) - \frac{\overline{f}_{V_0} f_w}{2\overline{R}}\overline{V}_j\cos(\gamma_j) = 0, \tag{16}$$

allows the removal of $\ddot{\overline{r}}$ from the system of equations. The ODE system is then reduced to a set of $2n+1$ equations, composed of Eq. (13) for the angular motion of the central spacecraft and the p equations of out of plane angular motion for each tether given by Eq. (16) and the analogous in plane angular motion p equations defined by Eq. (15). This system is dependent of the minimum set of $1+2p$ generalized coordinates given by ϕ, $\boldsymbol{\gamma}_{p\times 1}$ and $\boldsymbol{\beta}_{p\times 1}$.

Furthermore, it's worth noting the interdependence between the dynamics of the central vehicle and the tethers, as well as the coupling of the dynamics of the movements outside the spinning plane, defined by γ_j, $\overline{V}_j$ and inside it, and linked to β_j, ϕ, and $\overline{M}_c$. In this latter case, it is evident that the significant difference between the available control actions, limited solely to $\overline{M}_c$, and the large number of states β_j (for $j = 1, \ldots, p$) plus ϕ, results in a very limited direct control capability. Consequently, more complex voltage modulations $\overline{V}_j$ are required to act on the tether's states associated with the motion in the spin plane. However, it's observed that these cross-effects are weighted by functions of $\sin(\gamma_j)$, diminishing their influence as the coning angle decreases.

Through manipulations, the nonlinear second-order ODE system, defined by Eq. (13), Eq. (15) and Eq. (16), can be expressed in the compact form

$$\mathbf{M}'(\overline{\mathbf{q}})\ddot{\overline{\mathbf{q}}} = \mathbf{f}'(\dot{\overline{\mathbf{q}}}, \overline{\mathbf{q}}, \overline{\mathbf{u}}), \tag{17}$$

where the vector of normalized generalized coordinates is $\overline{\mathbf{q}} = \begin{bmatrix} \phi & \boldsymbol{\gamma}^\top & \boldsymbol{\beta}^\top \end{bmatrix}^\top$, the vector of normalized controls is given by $\overline{\mathbf{u}} = \begin{bmatrix} \overline{M}_c & \overline{\mathbf{V}}^\top \end{bmatrix}^\top$ and $\mathbf{M}(\overline{\mathbf{q}})'$ represents the mass matrix of the system. Furthermore, the first order representation of the ODE system can be achieved by defining $\overline{\mathbf{x}} = \begin{bmatrix} \dot{\overline{\mathbf{q}}}^\top & \overline{\mathbf{q}}^\top \end{bmatrix}^\top = \begin{bmatrix} \dot{\phi} & \dot{\boldsymbol{\gamma}}^\top & \dot{\boldsymbol{\beta}}^\top & \phi & \boldsymbol{\gamma}^\top & \boldsymbol{\beta}^\top \end{bmatrix}^\top$ and can be written as

$$\dot{\overline{\mathbf{x}}} = \mathbf{M}(\overline{\mathbf{x}})^{-1}\,\mathbf{f}(\overline{\mathbf{x}}, \overline{\mathbf{u}}), \tag{18}$$

where

$$\mathbf{M}(\overline{\mathbf{x}}) = \begin{bmatrix} \mathbf{M}(\overline{\mathbf{x}})' & \mathbf{0} \\ \mathbf{0} & \mathbf{I} \end{bmatrix}, \qquad \mathbf{f}(\overline{\mathbf{x}}, \overline{\mathbf{u}}) = \begin{bmatrix} \mathbf{f}'(\overline{\mathbf{x}}, \overline{\mathbf{u}})^\top & \dot{\phi} & \dot{\boldsymbol{\gamma}}^\top & \dot{\boldsymbol{\beta}}^\top \end{bmatrix}^\top. \tag{19}$$

3. Problem formulation

This section presents the formulation of the stable transition problem between two operational steady-state conditions of an E-sail. Firstly, the steady-state concept is defined, and a brief overview is provided of how different configuration parameters and operating regimes characterize this steady-state condition. Secondly, the transition between two different steady-states is studied considering two phases: the maneuver planning phase, where the open-loop control law is computed to execute the optimal transition, and the tracking phase, in which the feedback control law is obtained to minimize the actual deviations of the system from the optimal planned trajectory previously established.

Following this process, the formulation of the dynamic inversion problem is addressed in Sect. 3.2, i.e., the computation of control signals that enable the transition from an initial steady state s_1 to a target state s_2. This is approached from the perspective of an optimal control problem, which is discretized to yield a Nonlinear Programming (NLP) problem. The control law obtained from it is called the open-loop optimal control law, and the corresponding evolution of variables is called the optimal reference trajectory. Note that the optimal transition is computed under nominal solar wind conditions. Due to factors such as discretization during the inversion phase or variability in solar wind magnitudes, applying the open-loop control law will not result in perfect tracking of the optimal reference trajectory. Hence, a closed-loop control strategy is required to enhance tracking, as discussed in Sect. 3.3. This closed-loop control law is computed using the MPC scheme, which shares the same optimal control problem framework used in inversion but resorts to solving a sequence of such problems where the cost function is formulated precisely based on the deviation from the optimal reference trajectory under realistic fluctuation of solar wind magnitudes. Further details regarding the presented aspects are provided in the following sections.

3.1. Steady operation

In this section, the concept of steady-state operation is defined. Additionally the impact of the main E-sail configuration parameters and operation regime in the steady-state condition is provided. The results presented in this section differs of those in [67] by the fact of not considering auxiliary tethers.

The steady operation condition of an E-sail is defined by the following conditions. Null angular accelerations, $\ddot{\overline{\boldsymbol{\gamma}}}_s = \ddot{\overline{\boldsymbol{\beta}}}_s = \mathbf{0}$ and $\ddot{\overline{\phi}}_s = 0$. Null tether angular velocities, $\dot{\overline{\boldsymbol{\gamma}}}_s = \dot{\overline{\boldsymbol{\beta}}}_s = \mathbf{0}$, and central spacecraft angular velocity equal to the nominal value $\dot{\overline{\phi}}_s = \dot{\overline{\phi}}_0$. Null lagging angle, $\beta_j = \mathbf{0}$, and uniform coning angle, $\gamma_j = \gamma_s$, for all the tethers. And constant linear acceleration of the E-sail $\ddot{\overline{r}}_s$. The application of previous conditions into Eq. (12) to (15) allows for obtaining the equilibrium controls, $\overline{M}_c = 0$ and given an acceleration $\ddot{\overline{r}}_s$, the values of $\overline{V}_s$ and γ_s are the solution of the following system of algebraic equations:

$$\begin{gathered} \ddot{\overline{r}}_s - p\,\overline{f}_{V_0} f_w\,\overline{V}_s\cos^2(\gamma_s) = 0 \\ \left(\overline{J}_{t+u}\sin(2\gamma_s) + \overline{m}_{t+u}\sin(\gamma_s)\right)\dot{\overline{\phi}}_s^2 + \frac{\ddot{\overline{r}}_s\,\overline{m}_{t+u}\cos(\gamma_s)}{\overline{R}_r} - \frac{\overline{f}_{V_0} f_w\,\overline{V}_s\cos(\gamma_s)}{\overline{R}_r} = 0 \end{gathered} \tag{20}$$

Solving for $\ddot{\overline{r}}_s$ from the first expression and substituting it into the second one, the following equation can be obtained, which allows for calculating γ_s given the operating condition and the parameters of the E-sail:

$$\left(\overline{J}_{t+u}\sin(2\gamma_s) + \overline{m}_{t+u}\sin(\gamma_s)\right)\dot{\overline{\phi}}_s^2 + \frac{\left(p\,\overline{m}_{t+u}\cos^2(\gamma_s) - 1\right)}{\overline{R}_r}\overline{f}_{V_0} f_w\,\overline{V}_s\cos(\gamma_s) = 0 \tag{21}$$

The equation involves variables of various orders of magnitude. Assuming average solar wind conditions $f_w = 1.00$, the consideration of the baseline configuration detailed in Table 1 allows to establish that $\overline{J}_{t+u}$ and $\overline{m}_{t+u}$ are of order 10 and 10^{-3}, respectively, $\overline{R}_r$ is typically of order 10^{-4} and $\overline{f}_{V_0}$ is of order 10^{-3}. Given that γ_s is of order 10^{-2}, the term $\left(\overline{m}_{t+u}\sin(\gamma_s)\right)$ can be disregarded with respect to $\left(\left(\overline{J}_{t+u}\sin(2\gamma_s)\right)\right)$. Similarly, $\left(p\,\overline{m}_{t+u}\cos^2(\gamma_s)\right)$ can be neglected compared to 1, and considering small angles approximation for γ_s, the Eq. (21) can be simplified to:

$$\overline{J}_{t+u}\,2\gamma_s\,\dot{\overline{\phi}}_s^2 \approx \frac{\overline{f}_{V_0}\,\overline{V}_s}{\overline{R}_r}, \tag{22}$$

leading to the following approximated expression of the equilibrium coning angle

$$\gamma_s \approx \frac{\overline{f}_{V_0}\,\overline{V}_s}{2\,\overline{R}_r\,\overline{J}_{t+u}\,\dot{\overline{\phi}}_s^2}. \tag{23}$$

The evolution of the solution of Eq. (20) for different variations in the main parameters of the E-sail relative to the baseline configuration is analyzed and depicted in Fig. 4, illustrating the impact on the equilibrium coning angle γ_s and the propulsive force generated, $F_s = \ddot{r}_s\,m_e$, during steady-state operation. The observed trends and evolutions in γ_s can be straightforwardly justified based on the approximate expression provided in Eq. (23).

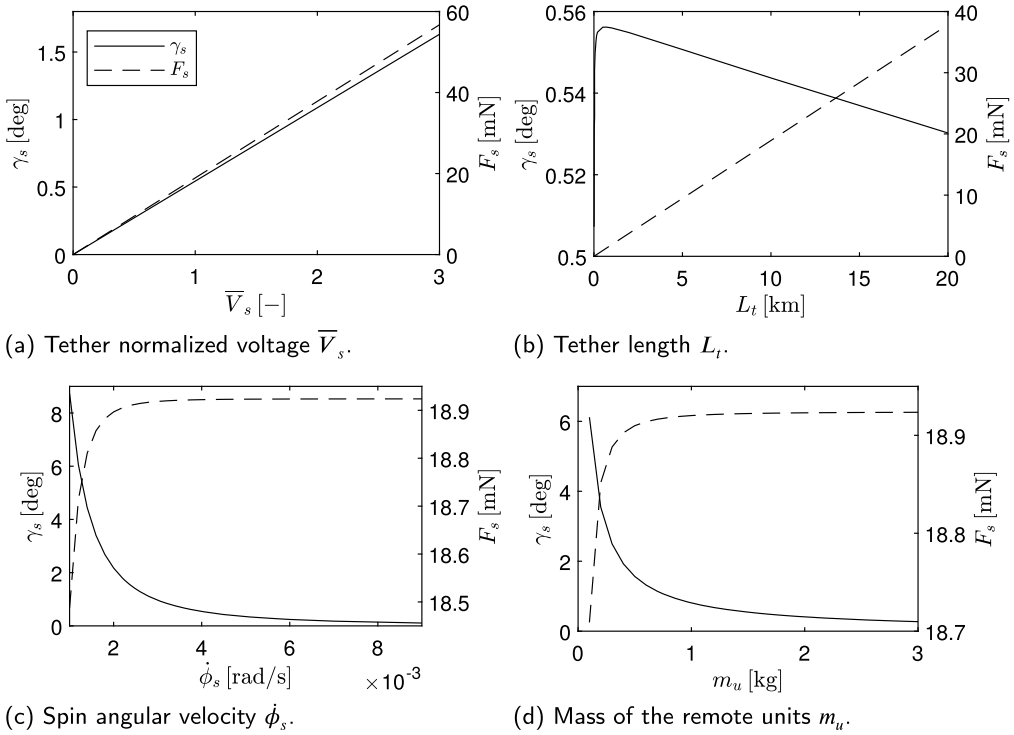

(a) Tether normalized voltage $\overline{V}_s$. (b) Tether length L_t.

(c) Spin angular velocity $\dot{\phi}_s$. (d) Mass of the remote units m_u.

Fig. 4. Description of the influence on the equilibrium coning angle γ_s and the generated propulsive force F_s for the baseline E-sail configuration.

In Fig. 4 (a), a linear and increasing evolution of both magnitudes with voltage is observed. It is noted how the equilibrium angle remains within an acceptably reduced range for the studied voltage range, corresponding to voltages between 0 and 60 kV. Regarding the effect of cable length L_t, Fig. 4 (b) shows how, beyond a minimum length, the evolution between equilibrium angle and length is linear, resulting in a slight reduction in the required angle. This modification is due to the increase in the dimensionless moment of inertia of the tether relative to the anchor point $\overline{J}_{t+u}$. Additionally, the observation of the results for the generated propulsive force shown in Fig. 4 (b) also demonstrates a linear and sustained growth with cable length. Regarding the effect of angular velocity, unlike the previously discussed parameters and consistent with the approximate expression given by Eq. (23), it has a non-linear impact with an asymptotic trend for both the equilibrium angle γ_s and the value of the generated propulsive force F_s, as observed Fig. 4 (c). Finally, regarding the impact of the mass of the remote unit m_u, given the low linear density of the tethers and their relatively light mass (approximately 100 grams for the baseline configuration), the mass of the remote unit significantly contributes to the moment of inertia $\overline{J}_{t+u}$ of the tether plus remote unit assembly (98% for the baseline configuration). Therefore, any increase/decrease in its mass leads to a notable increase/reduction in the moment of inertia, respectively. This phenomenon justifies the hyperbolic evolution observed for γ_s and F_s in Fig. 4 (d).

3.2. Transition maneuver optimal planning

In this section, the formulation of the inversion problem to compute the control law enabling a stable transition between the initial and target steady-states is introduced. The method considered for the inversion of the non-linear E-sail dynamical model established in Sect. 2, is based on an optimal control approach and employs a direct transcription method to solve the optimal control problem (OCP) formulated [68]. This approach offers the advantage of not requiring the derivation of internal dynamic equations and can be applied to multibody dynamics formulations in DAE form, which are widely used in the MBS field for defining complex multibody models that may include both rigid and flexible elements [9].

Given an E-sail in an initial steady-state, defined according to Sect. 3.1 and denoted as s_1, with the objective of evolving towards a target steady-state defined as s_2, the stable transition maneuver between the two states, t_{12}, is defined as the process that adjusts the states values from their initial to target values while keeping them within bounded ranges throughout the maneuver, as described in Fig. 5. Initially, there is a stage of duration $\overline{t}_{s_1}$, where the E-sail starts from the steady-state s_1, characterized by an angular velocity $\dot{\overline{\phi}}_{s_1} = \dot{\overline{\phi}}_0$ and a constant and uniform coning angle γ_{s_1} associated with a voltage modulation $\overline{V}_{s_1}$. This is followed by the transition stage of duration $\overline{t}_m$, during which the system evolves within defined bounds. The maneuver concludes with a final stage of duration $\overline{t}_{s_2}$, where the E-sail reaches the target steady-state s_2, characterized by the same angular velocity $\dot{\overline{\phi}}_{s_2} = \dot{\overline{\phi}}_0$ and a constant and uniform coning angle γ_{s_2} associated with a voltage modulation $\overline{V}_{s_2}$. It is important to note that, in order to keep the state evolution bounded throughout the transition, a reference trajectory must be established. This trajectory is represented in Fig. 5 as the steady-state values connected by a ramp, but it will be described in more detail later in Sect. 3.2.2.

The control inputs considered to achieve this transition are: the central vehicle control moment $\overline{M}_c$ and the variation of Coulomb forces associated with voltage modulation $\overline{\mathbf{V}}$. This approach results in an under-actuated system where the number of controls $1 + p$ is lower than to the number of generalized coordinates, given by ϕ, $\boldsymbol{\gamma}$ and $\boldsymbol{\beta}$. Additionally, for the computation of the optimal planning, a constant solar wind is assumed, characterized by average conditions such as a density n_{w0} and velocity u_{w0}, in accordance with Sect. 2.2.1.

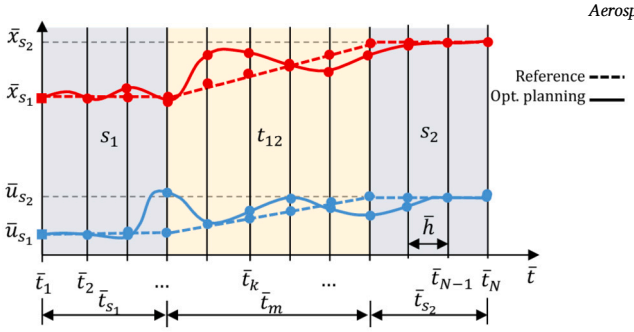

Fig. 5. Description of optimal control problem for the optimal planning of the transition of an E-sail between the initial steady-state s_1 to the target steady-state s_2.

3.2.1. The optimization problem

Given the dynamics of the system, defined by a system of nonlinear differential equations as described in Eqs. (18), the objective of optimal control is to compute the evolution of control magnitudes between initial time $\bar{t}_i$ and final time $\bar{t}_f$, minimizing a cost function of the form

$$\mathcal{J} = \int_{\bar{t}_0}^{\bar{t}_f} \mathscr{L}\left(\bar{\mathbf{x}}(\bar{t}), \bar{\mathbf{u}}\left(\bar{t}\right)\right) d\bar{t} + \mathscr{E}\left(\bar{\mathbf{x}}\left(\bar{t}_f\right), \bar{\mathbf{u}}\left(\bar{t}_f\right)\right), \tag{24}$$

where $\mathscr{L}$ represent the Lagrange term of the cost function defined during the interval $[\bar{t}_i, \bar{t}_f]$ and $\mathscr{E}$ is the Mayer term, which is function of the terminal states. This minimization is subjected to a set of constraints, which in this case are considered to be equality constraints and may have different origins. These constraints may be associated with the system's own dynamic equations, compliance with permissible ranges of values for states and controls, or tracking a certain trajectory for some states. In a compact form, these constraints can be written as

$$\mathbf{c}\left(\bar{\mathbf{x}}(t), \bar{\mathbf{u}}(t)\right) = \mathbf{0}. \tag{25}$$

Among all the alternatives for solving optimization problems: dynamic programming [69], indirect methods [70], and direct methods [71,72], this work opts for the latter. Specifically, a direct transcription method is chosen, allowing the problem to be rewritten in discrete form, resulting in an NLP, described in Fig. 5, where both the states and control signals are computed simultaneously in order to optimize the cost function and satisfy the constraints. Considering that the time interval between $\bar{t}_i$ and $\bar{t}_f$ is divided into N discretization points, defining $N-1$ subintervals of dimensionless duration $\bar{h} = (\bar{t}_f - \bar{t}_i)/(N-1)$. The vector of design variables of the optimization problem can be established as

$$\bar{\mathbf{X}} = \left(\bar{\mathbf{x}}_1; \bar{\mathbf{u}}_1; \ldots; \bar{\mathbf{x}}_k; \bar{\mathbf{u}}_k; \ldots; \bar{\mathbf{x}}_N; \bar{\mathbf{u}}_N\right), \tag{26}$$

being $\bar{\mathbf{x}}_k$ and $\bar{\mathbf{u}}_k$ the vectors of system states and controls at the $k-$th discretization point, respectively. Additionally, in order to ensure proper conditioning of the optimization problem, normalization of design variables and constraint functions is conducted by establishing normalization factors for each of the states and equations. Thus, considering the typical orders of magnitude of the states in position and velocity, as well as the controls and constraints, normalization factor vectors are defined as

$$\mathbf{f}_x = \left[f_{\dot{\phi}} \quad \mathbf{f}_{\dot{\gamma}}^\top \quad \mathbf{f}_{\dot{\beta}}^\top \quad f_\phi \quad \mathbf{f}_\gamma^\top \quad \mathbf{f}_\beta^\top\right], \mathbf{f}_u = \left[f_{M_c} \quad \mathbf{f}_V\right], \mathbf{f}_{\dot{x}} = \left[f_{\ddot{\phi}} \quad \mathbf{f}_{\ddot{\gamma}} \quad \mathbf{f}_{\ddot{\beta}} \quad f_{\dot{\phi}} \quad \mathbf{f}_{\dot{\gamma}} \quad \mathbf{f}_{\dot{\beta}}\right], \tag{27}$$

being f_y the normalization factor associated to the state or control y.

3.2.2. Objective function

The following discrete objective function is established containing terms associated with the states $\bar{\mathbf{x}}_k = \left[\bar{\dot{\mathbf{q}}}_k^\top \quad \bar{\mathbf{q}}_k^\top\right]^\top$, as well as the controls $\bar{\mathbf{u}}_k$, in terms of normalized variables:

$$\mathcal{J}^d = \sum_{k=1}^{N-1} \bar{h}\left(\hat{\mathbf{x}}_k^\top \mathbf{\Lambda}_k \hat{\mathbf{x}}_k + \hat{\mathbf{u}}_k^\top \mathbf{\Sigma}_k \hat{\mathbf{u}}_k\right) + \hat{\mathbf{x}}_N^\top \mathbf{\Lambda}_N \hat{\mathbf{x}}_N + \hat{\mathbf{u}}_N^\top \mathbf{\Sigma}_N \hat{\mathbf{u}}_N, \tag{28}$$

where the variables $\hat{}$ represent the normalized error of the magnitudes with respect to the reference values. In this way, normalized error on the system states is established as

$$\hat{\mathbf{x}}_k = \left(\bar{\mathbf{x}}_k - \bar{\mathbf{x}}_k^r\right) \oslash \mathbf{f}_x, \tag{29}$$

and the normalized error on control inputs as

$$\hat{\mathbf{u}}_k = \left(\bar{\mathbf{u}}_k - \bar{\mathbf{u}}_k^r\right) \oslash \mathbf{f}_u. \tag{30}$$

Equations in which, $\oslash$ represents the Hadamard division, also known as element-wise division defined for two vectors of n components as: $\mathrm{a} \oslash \mathrm{b} = \left(a_1/b_1, a_2/b_2, \ldots a_n/b_n\right)$.

The state and control references are defined as a function of the time instant associated with point k, for $k = 1, \ldots, N$, being established depending on whether the time instant belongs to the initial steady-state, s_1, the transient or maneuvering interval, t_{12}, or the target steady-state s_2. In this way, the references are defined as

$$\overline{\mathbf{x}}_k^r = \begin{cases} \begin{bmatrix} \dot{\overline{\phi}}_0 & \mathbf{0}^\top & \mathbf{0}^\top & \ddot{\overline{\phi}}_0 \overline{t}_k & \boldsymbol{\gamma}_{s_1}^\top & \mathbf{0}^\top \end{bmatrix}^\top & \text{if } \overline{t}_k \le \overline{t}_{s_1} \\ \begin{bmatrix} \dot{\overline{\phi}}_0 & \mathbf{0}^\top & \mathbf{0}^\top & \ddot{\overline{\phi}}_0 \overline{t}_k & \boldsymbol{\gamma}_{s_1}^\top + \frac{\left(\overline{t}_k - \overline{t}_{s_1}\right)\left(\boldsymbol{\gamma}_{s_2}^\top - \boldsymbol{\gamma}_{s_1}^\top\right)}{\overline{t}_m} & \mathbf{0}^\top \end{bmatrix}^\top & \text{if } \overline{t}_{s_1} < \overline{t}_k \le \overline{t}_{s_1} + \overline{t}_m \\ \begin{bmatrix} \dot{\overline{\phi}}_0 & \mathbf{0}^\top & \mathbf{0}^\top & \ddot{\overline{\phi}}_0 \overline{t}_k & \boldsymbol{\gamma}_{s_2}^\top & \mathbf{0}^\top \end{bmatrix}^\top & \text{if } \overline{t}_{s_1} + \overline{t}_m < \overline{t}_k \le \overline{t}_{s_1} + \overline{t}_m + \overline{t}_{s_2} \end{cases}$$

$$\overline{\mathbf{u}}_k^r = \begin{cases} \begin{bmatrix} 0 & \overline{\mathbf{V}}_{s_1}^\top \end{bmatrix}^\top & \text{if } \overline{t}_k \le \overline{t}_{s_1} \\ \begin{bmatrix} 0 & \overline{\mathbf{V}}_{s_1}^\top + \frac{\left(\overline{t}_k - \overline{t}_{s_1}\right)\left(\overline{\mathbf{V}}_{s_2}^\top - \overline{\mathbf{V}}_{s_1}^\top\right)}{\overline{t}_m} \end{bmatrix}^\top & \text{if } \overline{t}_{s_1} < \overline{t}_k \le \overline{t}_{s_1} + \overline{t}_m \\ \begin{bmatrix} 0 & \overline{\mathbf{V}}_{s_2}^\top \end{bmatrix}^\top & \text{if } \overline{t}_{s_1} + \overline{t}_m < \overline{t}_k \le \overline{t}_{s_1} + \overline{t}_m + \overline{t}_{s_2} \end{cases} \tag{31}$$

where $\overline{t}_k = (k-1)\,\overline{h}$. Furthermore, the weighting matrices of the objective function, which have a diagonal structure, are defined as $\boldsymbol{\Lambda}_j = \mathrm{diag}(\mathbf{v}\boldsymbol{\Lambda}_j)$ and $\boldsymbol{\Sigma}_j = \mathrm{diag}(\mathbf{v}\boldsymbol{\Sigma}_j)$, for $j = s_1, t_{12}, s_2$, where the weight vectors are given by $\mathbf{v}\boldsymbol{\Lambda} = \begin{bmatrix} \Lambda_{\dot{\phi}} & \boldsymbol{\Lambda}_{\dot{\gamma}}^\top & \boldsymbol{\Lambda}_{\dot{\beta}}^\top & \Lambda_{\phi} & \boldsymbol{\Lambda}_{\gamma}^\top & \boldsymbol{\Lambda}_{\beta}^\top \end{bmatrix}^\top$ for the states and their derivatives, and by $\mathbf{v}\boldsymbol{\Sigma} = \begin{bmatrix} \Sigma_{M_c} & \boldsymbol{\Sigma}_V^\top \end{bmatrix}^\top$ for the controls.

3.2.3. Constraints functions

The optimal control perspective considered in this work for the dynamic inversion problem, allows the straightforward consideration of the constraints associated to: the integration method, the permissible ranges for states and control values or the application of boundary conditions, between others. In this application, the constraints $\mathbf{c}_{d_k}$, which enforce compliance with the system's dynamic equations, and the boundary condition constraints at the initial point $\mathbf{c}_{b_1}$, are treated as optimization constraints. Meanwhile, the permissible ranges for states and controls are used to limit the search domain. Therefore, the vector of normalized optimization constraints is defined as $\hat{\mathbf{c}} = \begin{bmatrix} \hat{\mathbf{c}}_{d_1}^\top & \hat{\mathbf{c}}_{d_2}^\top & \cdots & \hat{\mathbf{c}}_{d_{N-1}}^\top & \hat{\mathbf{c}}_{b_1}^\top \end{bmatrix}^\top$.

The constraints $\mathbf{c}_{d_k}$, given by the integration scheme and defined in this case by a fourth-order Runge-Kutta algorithm, establish $1+2p$ nonlinear equations at $N-1$ instants, resulting in $(1+2p)(N-1)$ equations, given by:

$$\mathbf{c}_{d_k} = \overline{\mathbf{x}}_{k+1} - \overline{\mathbf{x}}_k - \frac{h}{6}(\mathbf{k}_1 + 2\mathbf{k}_2 + 2\mathbf{k}_3 + \mathbf{k}_4) \tag{32}$$

for $k = 1, .., N-1$, where according to the selected scheme and Eq (18):

$$\begin{aligned} \mathbf{k}_1 &= \mathbf{M}^{-1}\mathbf{f}(\overline{\mathbf{x}}_k, \overline{\mathbf{u}}_k), \\ \mathbf{k}_2 &= \mathbf{M}^{-1}\mathbf{f}(\overline{\mathbf{x}}_k + \overline{h}\,\mathbf{k}_1/2, (\overline{\mathbf{u}}_{k+1} + \overline{\mathbf{u}}_k)/2, \\ \mathbf{k}_3 &= \mathbf{M}^{-1}\mathbf{f}(\overline{\mathbf{x}}_k + \overline{h}\,\mathbf{k}_2/2, (\overline{\mathbf{u}}_{k+1} + \overline{\mathbf{u}}_k)/2, \\ \mathbf{k}_4 &= \mathbf{M}^{-1}\mathbf{f}(\overline{\mathbf{x}}_k + \overline{h}\,\mathbf{k}_3, \overline{\mathbf{u}}_{k+1}). \end{aligned} \tag{33}$$

And at each instant, the normalized constraints associated with the integrator are established as:

$$\hat{\mathbf{c}}_{d_k} = \mathbf{c}_{d_k} \oslash \mathbf{f}_{\dot{x}}. \tag{34}$$

In addition to the previous constraints, the constraints associated with imposing boundary conditions at the initial instant, impose $1+2\,p$ additional constraints and are also defined in a normalized manner as:

$$\hat{\mathbf{c}}_{b_1} = \mathbf{c}_{b_1} \oslash \begin{bmatrix} \mathbf{f}_{\mathbf{x}} \\ \mathbf{f}_{\mathbf{u}} \end{bmatrix}, \tag{35}$$

where $\oslash$ represents the Hadamard division and $\mathbf{c}_{b_1} = \begin{bmatrix} \left(\overline{\mathbf{x}}_1 - \overline{\mathbf{x}}_i\right)^\top & \left(\overline{\mathbf{u}}_1 - \overline{\mathbf{u}}_i\right)^\top \end{bmatrix}^\top$, being $\overline{\mathbf{x}}_i$ and $\overline{\mathbf{u}}_i$ the initial conditions for states and controls.

Finally the upper and lower bounds of the design variables are established by the definition of the normalized upper and lower values for the design variables. The upper and lower bounds $\overline{\mathbf{v}}_{lb_k}$ and $\overline{\mathbf{v}}_{ub_k}$ for the design variables are considered identical for all time instants and are defined for $k = 1, ..., N$ by:

$$\begin{aligned} \overline{\mathbf{v}}_{lb_k} &= \begin{bmatrix} lb_{\dot{\phi}} & \mathbf{lb}_{\dot{\gamma}} \mathbf{1}_{p\times 1}^\top & \mathbf{lb}_{\dot{\beta}}^\top & lb_{\phi} & \mathbf{lb}_{\gamma}^\top & \mathbf{lb}_{\beta}^\top & lb_{M_c} & \mathbf{lb}_V^\top \end{bmatrix}^\top \oslash \begin{bmatrix} \mathbf{f}_{\mathbf{x}}^\top & \mathbf{f}_{\mathbf{u}}^\top \end{bmatrix}^\top, \\ \overline{\mathbf{v}}_{ub_k} &= \begin{bmatrix} ub_{\dot{\phi}} & \mathbf{ub}_{\dot{\gamma}}^\top & \mathbf{ub}_{\dot{\beta}}^\top & ub_{\phi} & \mathbf{ub}_{\gamma}^\top & \mathbf{ub}_{\beta}^\top & ub_{M_c} & \mathbf{ub}_V^\top \end{bmatrix}^\top \oslash \begin{bmatrix} \mathbf{f}_{\mathbf{x}}^\top & \mathbf{f}_{\mathbf{u}}^\top \end{bmatrix}^\top. \end{aligned} \tag{36}$$

3.2.4. Initial iterant and resolution

The initial iterate supplied consists of the initial reference values for the states, their derivatives, and the controls established in Eqs. (31).

The solution obtained for the OCP, $\overline{\mathbf{X}}^p$ is referred to as optimal planning, from which the optimal trajectory for the states, $\overline{\mathbf{x}}^p(\overline{t}_k)$, and the open-loop optimal control law, $\overline{\mathbf{u}}^p(\overline{t}_k)$, can be extracted at the discretization points for $k = 1, ..., N$.

3.3. Transition tracking MPC control

In this section, the tracking problem of an E-sail during the execution of the optimal transition maneuver between two equilibrium states, as described in Sect. 3.2, is analyzed. The application of an open-loop optimal control law, in the presence of disturbances and uncertainties, does not

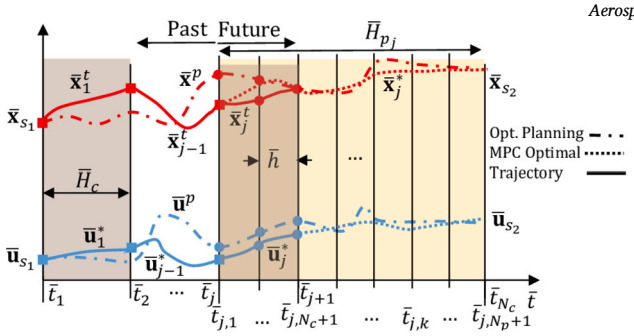

Fig. 6. Description of Model Predictive Control application for E-sail transition tracking.

guarantee that the system precisely follows the planned trajectory, thus requiring feedback to ensure accurate tracking of the optimal trajectory. Given that this is a theoretical study, there is no distinction between a dynamic model used for prediction and a real system from which to obtain the trajectory. Instead, both are dynamic models that differ in the solar wind equivalent factor considered. For predictions, $\overline{\mathbf{x}}$, a constant solar wind factor equal to the one measured at the start of the prediction is used, while for trajectory calculation, $\overline{\mathbf{x}}^t$, the temporal evolution of the solar wind equivalent factor is considered, providing a more realistic representation of associated disturbances. This, along with the effects of the discretization used in solving the planning problem, necessitates the application of a feedback law to minimize deviations from the optimal trajectory. For this purpose, the use of MPC techniques is proposed. This approach involves solving successive optimal control problems, where, based on the states and the solar wind factor measured at a given instant, the control actions are recalculated using a system dynamics model to minimize the deviation of the predicted trajectory from the previously established optimal plan. This process is illustrated in Fig. 6 for the specific transition tracking scenario. Given the similarities with the planning formulation described in Sect. 3.2, this scheme shares the benefit of not requiring the derivation of internal dynamic equations and can be adapted for other more detailed formulations of E-sail multibody dynamics expressed in DAE form. Additionally, it is not restricted to differentially flat or minimum phase systems, but it is also suitable for non-minimum phase systems. In coherence with the optimal planning described in Sect. 3.2, only the variation of Coulomb forces due to voltage modulation $\overline{\mathbf{V}}$ and the central vehicle control moment $\overline{M}_c$ are considered for actuation, resulting in an under-actuated system.

3.3.1. *The feedback problem statement*

Considering the dynamic model established in Sect. 2, the problem of calculating a feedback control law that ensures the tracking of the optimal transition trajectory, as defined in Sect. 3.2, is posed.

Considering a time instant $\bar{t}_j$ at which the system states $\overline{\mathbf{x}}^t(\bar{t}_j)$ are known, and assuming the evolution of the solar wind equivalent factor $f_w(\bar{t})$ is also known, the trajectory followed by the E-sail states $\overline{\mathbf{x}}^t_j(\bar{t})$, can be calculated by considering a given control law $\overline{\mathbf{u}}^*_j(\bar{t})$ and the time evolution of the solar wind magnitudes. However, after a certain period, called the control horizon, at instant $\bar{t}_{j+1} < \bar{t}_f$, it is assumed that the solar wind factor $f_w(\bar{t}_{j+1})$ and the system states can be measured, and the difference between the measured state $\overline{\mathbf{x}}^t_j(\bar{t}_{j+1})$ and the state specified by the optimal trajectory $\overline{\mathbf{x}}^p(\bar{t}_{j+1})$ can be calculated. Considering the following prediction period, starting at the instant of the new measurement $\bar{t}_{j+1}$ and ending always at $\bar{t}_f$, a new control law $\overline{\mathbf{u}}^*_{j+1}(\bar{t})$ can be computed under the assumption that the solar wind factor remains constant and equal to the last measurement. This feedback control law is optimal in the sense that, based on the predicted evolution of the system, it minimizes a cost function associated with the deviation of the system's states from the optimal planned trajectory, $\overline{\mathbf{x}}^p(\bar{t})$, over the remaining transition time, which defines the prediction horizon. This approach defines the optimal control technique known as Model Predictive Control (MPC) [73]. Given that the final instant is fixed and considering that as time progresses, each new measurement is taken closer to the final instant, resulting in a progressively shorter prediction horizon, this approach is referred to as Shrinking Horizon Model Predictive Control (SHMPC).

Similarly to Sect. 3.2.2, the optimal control problem is stated as the minimization of the cost function established by,

$$\mathcal{J}^d = \sum_{k=1}^{N_p+1} \overline{h}\left(\hat{\mathbf{x}}_k^\top \mathbf{\Lambda}_k \hat{\mathbf{x}}_k + \hat{\mathbf{u}}_k^\top \mathbf{\Sigma}_k \hat{\mathbf{u}}_k + \Delta\hat{\boldsymbol{\gamma}}_k^\top \mathbf{\Lambda}_{\Delta\gamma_k} \Delta\hat{\boldsymbol{\gamma}}_k + \Delta\hat{\boldsymbol{\beta}}_k^\top \mathbf{\Lambda}_{\Delta\beta_k} \Delta\hat{\boldsymbol{\beta}}_k\right) + \hat{\mathbf{x}}_N^\top \mathbf{\Lambda}_N \hat{\mathbf{x}}_N + \hat{\mathbf{u}}_N^\top \mathbf{\Sigma}_N \hat{\mathbf{u}}_N, \tag{37}$$

evaluated between $\bar{t}_{j+1}$ and $\bar{t}_f$, where the variables $\hat{}$ represent the normalized error of the magnitudes. In this way, normalized error on the system states with respect to the optimal planned transition as

$$\hat{\mathbf{x}}_k = \left(\overline{\mathbf{x}}_k - \overline{\mathbf{x}}^p_k\right) \oslash \mathbf{f}_x, \tag{38}$$

and the normalized error on control inputs as

$$\hat{\mathbf{u}}_k = \left(\overline{\mathbf{u}}_k - \overline{\mathbf{u}}^p_k\right) \oslash \mathbf{f}_u. \tag{39}$$

Moreover, the contributions associated with $\Delta\hat{\boldsymbol{\gamma}}_k$ and $\Delta\hat{\boldsymbol{\beta}}_k$ include in the cost function the deviations of the angular positions of one tether relative to others, thus effectively addressing operation under non-homogeneous conditions. The vector of deviations for γ, with dimension $(p-1)!$, is defined as:

$$\Delta\hat{\boldsymbol{\gamma}}_k = \left[(\gamma_2-\gamma_1) \quad (\gamma_3-\gamma_1) \quad \cdots \quad (\gamma_{p-1}-\gamma_1) \quad (\gamma_p-\gamma_1) \quad (\gamma_3-\gamma_2) \quad \cdots \quad (\gamma_p-\gamma_1) \quad \cdots \quad (\gamma_p-\gamma_{p-1})\right]^\top / f_\gamma, \tag{40}$$

and for β, it can be written as:

$$\Delta\hat{\boldsymbol{\beta}}_k = \left[(\beta_2-\beta_1) \quad (\beta_3-\beta_1) \quad \cdots \quad (\beta_{p-1}-\beta_1) \quad (\beta_p-\beta_1) \quad (\beta_3-\beta_2) \quad \cdots \quad (\beta_p-\beta_1) \quad \cdots \quad (\beta_p-\beta_{p-1})\right]^\top / f_\beta, \tag{41}$$

In addition, the compliance with the constraints defined by the equations associated with the time integration scheme, described in Sect. 3.2.3, must be ensured, and the initial boundary conditions given by the state measurements must be satisfied.

In regard to the OCP resolution, the approach proposed in Sect. 3.2 for the planning is also followed, where the successive optimization problems are discretized, resulting in a series of NLPs defined as follows. Given the transition process of an E-sail between two steady states, an analysis period $\overline{H}_o$ is defined between the initial time $\bar{t}_i$ and final time $\bar{t}_f$. A time discretization $\overline{h}$ is established, and the control horizon N_c is set as the number of discretizations intervals of duration $\overline{h}$, that defines the separation between state and solar wind parameter measurements (which are assumed to be synchronized) and during which the feedback control law obtained from the previous iteration will be applied. Thus, the duration of the control horizon will be $\overline{H}_c = N_c\,\overline{h}$, and assuming that $\overline{h}$ is defined such that $\overline{H}_o$ is an integer multiple of $\overline{H}_c$, it can be calculated that $N_o = \overline{H}_o/\overline{H}_c$ feedback laws will be required. Each of these laws will be calculated at the instant $\bar{t}_j$, for $j = 1, ..., N_o$, and will be obtained as the one that minimizes the deviation from the planned optimal trajectory between the instant $\bar{t}_j$, when the states and solar wind are measured, and the instant $\bar{t}_f$, when the transition ends. The prediction horizon for the j-th optimization problem is defined as having a duration given by $\overline{H}_{p_j} = \overline{H} - \overline{H}_c(j-1)$ and the NLP to be solve has $N_{p_j} + 1$ discretization points, being $N_{p_j} = \overline{H}_{p_j}/\overline{h}$. Taking all of the above into account, the establishment of the j-th optimal control problem considers a new discretization into N_{p_j} subintervals, each with a duration $\overline{h}$, defining the instants $\bar{t}_{j,k}$, for $k = 1, ..., N_{p_j} + 1$, such that $\bar{t}_{j,1} = \bar{t}_j$ and $\bar{t}_{j,N_{p_j}+1} = \bar{t}_f$. The design variable vector of the j-th OCP is defined as

$$\overline{\mathbf{X}}_j = \left(\overline{\mathbf{x}}_{j,1}; \overline{\mathbf{u}}_{j,1}; \dots; \overline{\mathbf{x}}_{j,k}; \overline{\mathbf{u}}_{j,k}; \dots; \overline{\mathbf{x}}_{j,N_{p_j}+1}; \overline{\mathbf{u}}_{j,N_{p_j}+1}\right). \tag{42}$$

Considering that $\overline{\mathbf{X}}_j^0$ is the initial iterant for solving the j-th OCP and $\overline{\mathbf{X}}_j^*$ is its optimal solution, from which the optimal control law $\overline{\mathbf{u}}_j^*$ can be extracted, and that $\overline{\mathbf{x}}_j^t$ represents the trajectory followed by the system during the j-th control interval under the application of the optimal control law and the actual solar wind evolution given by $f_w(\bar{t})$, the RHMPC procedure proposed can be described as the repetition, for $j = 1, \dots, N_o$, of the following steps:

1. At instant $\bar{t}_j$ (noting that $\bar{t}_j = \bar{t}_{j,1} = \bar{t}_{j-1,N_c+1}$) establish the boundary conditions for the system states and controls as: $\overline{\mathbf{x}}_{i_j} = \overline{\mathbf{x}}_{j-1}(\bar{t}_{j,1})$ and $\overline{\mathbf{u}}_{i_j} = \overline{\mathbf{u}}^*_{j-1}(\bar{t}_{j,1})$, and measure the solar wind equivalent factor f_{w_j}.
2. Compute the initial iterate $\overline{\mathbf{X}}_j^0$ based on the time forward integration, between $\bar{t}_j$ and $\bar{t}_f$ (noting that $\bar{t}_f = \bar{t}_{j,N_{p_j}+1}$), of the system dynamical equations given in Eq. (18), considering the boundary conditions $\overline{\mathbf{x}}_{i_j}$ and the control law given by the linear interpolation of $\overline{\mathbf{u}}^*_{j-1}$ and assuming a constant equivalent solar wind factor equal to f_{w_j}.
3. Use $\overline{\mathbf{X}}_j^0$ as initial iterate to solve the j-th OCP considering the cost function established in Eq. (37), based on the error of dimensionless states and controls in Eqs. (38) and (39) while enforcing the normalized dynamic constraints described in Eq. (34), the boundary conditions $\overline{\mathbf{x}}_{j,1} = \overline{\mathbf{x}}_{i_j}$ and $\overline{\mathbf{u}}_{j,1} = \overline{\mathbf{u}}_{i_j}$, and assuming a constant equivalent solar wind factor equal to f_{w_j}. This yields the design variables solution $\overline{\mathbf{X}}_j^*$, from which a new optimal control law $\overline{\mathbf{u}}_j^*$ and trajectory $\overline{\mathbf{x}}_j^*$ defined discretely at the instants $\bar{\mathbf{t}}_{j,k}$ for $k = 1, \dots, N_p + 1$ can be extracted.
4. Calculate the system trajectory $\overline{\mathbf{x}}_j^t(\bar{t})$ from the time forward integration between $\bar{t}_j = \bar{t}_{j,1}$ and $\bar{t}_{j+1} = \bar{t}_{j,N_c+1}$ of the system's dynamic equations described in Eq. (18), considering the boundary conditions $\overline{\mathbf{x}}_{i_j}$, the interpolation of the optimal control law $\overline{\mathbf{u}}_j^*$ and the time evolution of the solar wind given by $f_w(\bar{t})$.

4. Numerical simulation

This section presents and discusses the results obtained for the resolution of the planning and tracking problems posed in Sect. 3.2 and Sect. 3.3, respectively.

For the simulations presented here, the configuration of the E-sail used corresponds to that described in Table 1 and includes four tethers. Regarding the duration of the transition phases described in Fig. 5, the intervals s_1 and s_2 are both set to $\bar{t}_{s_1} = \bar{t}_{s_2} = 0.25$. Given the nominal spin rate defined in Table 1, this corresponds to approximately 392 seconds. Additionally, the initial voltage modulation, $\overline{V}_{s_1}$, is considered to be zero for all the tethers, although the procedure is applicable for different initial values. In Sect. 4.1 the results presented demonstrate the feasibility of performing the transition between two steady-states by controlling the evolution of the states solely through voltage modulation and central vehicle control. The impact of key parameters of the transition maneuver, the final voltage $\overline{V}_{s_2}$ and the transition time $\bar{t}_m$, on the optimal trajectory obtained is also presented. Additionally, the evolution of the maximum control requirements in relation to these parameters is provided. After analyzing the optimal planning, Sect. 4.2 presents the tracking results, demonstrating the effectiveness of MPC in this application and detailing the results for different planning scenarios. In addition to assess the validity of the proposed procedure under realistic solar wind fluctuations an non homogeneous tether configurations, the results of a Monte Carlo analysis are provided in which realistic solar wind fluctuations obtained from Enlil model [74] and random initial deviations of tethers positions respect to nominal steady-state are considered.

In relation to the resolution of the optimal control problems formulated in the previous sections, they are solved using the *fmincon* function in MATLAB R2023b, employing the interior point algorithm [75]. The functions for computing the nonlinear equality constraints and the objective function are provided to the algorithm, while the gradient of the objective and the Jacobian matrix of the constraint vector are not analytically provided but computed by the function itself using finite differences. As an example of the implementation's performance, indicate that for the transition from $\overline{V}_{s_1} = 0.0$ to $\overline{V}_{s_2} = 0.2$ with $\bar{t}_m = 1.0$, the number of function calls required for the planning phase and for the first tracking iteration are 796282 and 76985, respectively, while the associated computing times are 952 and 480 seconds.

In order to systematically and clearly establish control objectives and representative initial perturbations, the acceptable errors for angular position and angular rates are established for control and planning problems. The values of the acceptable control errors are set based on reasonable deviations (2%) from the nominal values associated with the baseline. The acceptable position error is established as 2% of the equilibrium coning angle γ_s, for a voltage modulation $\overline{V}_s = 1.0$. Following the description in Sec. 3.1, it can be demonstrated that this is approximately equal to 0.5

Table 2
Description of acceptable states errors.

Magnitude	Angular Position Error ϵ [°]	Angular velocity Error $\dot{\epsilon}$ [rad/s]
Acceptable Control Error, $_{\epsilon}$	$\pm 1 \cdot 10^{-2}$	$\pm 8 \cdot 10^{-5}$
Acceptable Planning Error, $_{p}$	$\pm 1 \cdot 10^{-5}$	$\pm 8 \cdot 10^{-8}$

Table 3
Definition of lower and upper bounds for states and controls for the transition between steady states with underactuation.

	$\dot{\phi}$	$\dot{\gamma}$	$\dot{\beta}$	ϕ	γ	β	M_c	V
lb	-10^1	-10^1	-10^1	-10^{-5}	-10^{-5}	-10^0	-10^{-5}	-10^0
ub	10^1	10^1	10^1	10^3	10^0	10^0	$2 \cdot 10^0$	10^0

Table 4
Definition of normalization factors considered for transition with underactuation.

Factor	$f_{\dot{\phi}}$	$f_{\dot{\gamma}}$	$f_{\dot{\beta}}$	f_{ϕ}	f_{γ}	f_{β}	f_{ϕ}	f_{γ}	f_{β}	f_{M_c}	f_V
Value	10^{-3}	10^{-2}	10^{-3}	2π	10^{-2}	10^{-3}	2π	10^{-3}	10^{-3}	10^0	10^0

Table 5
Definition of the weight factor for the cost function during the transition between steady states with underactuation.

	$\Lambda_{\dot{\phi}}$	$\Lambda_{\dot{\gamma}}$	$\Lambda_{\dot{\beta}}$	Λ_{ϕ}	Λ_{γ}	Λ_{β}	Σ_{M_c}	Σ_V
i = s_1, s_2	1.00	1.00	1.00	1.00	100.00	100.00	50.00	10.00
i = t	0.00	0.00	0.00	0.00	0.00	0.00	1.00	1.00

degrees for the baseline configuration. Consequently, the acceptable angular position error is set to $\epsilon_c = 0.01°$. Similarly, the acceptable error in angular velocity is established as 2% of $\dot{\phi}_0$, which corresponds to $\dot{\epsilon}_c = 8 \cdot 10^{-5}$ rad/s. It is important to emphasize that acceptable control errors considered should realistically reflect the errors associated with the measurement/estimation of the states using specific sensors. This estimation or measurement is necessary for calculating the feedback control law, and the errors are tied to the precision of the sensors used for the actual operation of the system. In this work, the acceptable control errors have been estimated and should be defined in later stages based on the specific characteristics of the sensors available and selected for the E-sail. Although the present work is quite far from implementation, it is verified that the established acceptable error values are consistent with the state-of-the-art in angular position sensors. For example, absolute rotary encoders such as the TONiC™ UHV REXM20 incremental encoder system, provided by Renishaw™, ensure accuracies of up to 1″ and compatible with operation in vacuum conditions. However, another situation arises during the maneuvers planning, such as the transition between steady-states presented in Sect. 3.2. It is crucial to understand that the planning phase is purely conceptual, whereas the tracking phase is the one that will be executed, where the acceptable control errors with respect to the optimal trajectory obtained in the planning will apply. The optimal planning solution, obtained in this work through the resolution of a cost function minimization problem defined in terms of the normalized state errors relative to a reference, must also satisfy acceptable error requirements. These planning errors should be significantly smaller than the control errors and are not limited by sensor precision since they are purely conceptual. Considering all the above, the Acceptable Planning Errors, ϵ_p and $\dot{\epsilon}_p$, are set to be three orders of magnitude smaller than the previously established control errors. The acceptable control and planning errors established are summarized in Table 2.

To conclude the overall definition of the upper and lower bounds for the system states and controls are considered identical for all time instants being their dimensional values are defined in Table 3.

4.1. Results for optimal transition planning

In this section, the results for the E-sail's optimal transition planning between two equilibrium states are presented. The specific values and parameters used for the simulations carried out are described and subsequently, the obtained results are presented and discussed.

The normalization factors considered for the normalization of OCP are outlined in Table 4, while the weights for the cost function are tailored to the specifications provided in Table 5. These values have been selected to fulfill the acceptable error requirements for planning, described in Table 2, considering the transition scenario defined by $\overline{V}_{s_1} = 0$, $\overline{V}_{s_2} = 0.2$, and $\bar{t}_m = 3.0$. It is important to highlight that while all states are uniformly penalized during the steady-state phases s_1 and s_2, during the transition, only the control inputs contribute to the overall cost function. The obtained results for the optimal solution are represented together with the initial iterant and the allowable errors in Fig. 7, from which the achievement of the error objectives for the planning phase can be concluded. Additionally, regarding the additional adjustments for solving the optimization problem, the tolerance of the constraints is set to 10^{-6}, the optimality tolerance of the cost function is set to 10^{-4}, and the maximum number of iterations is set to 800. A discretization considering 30 points per revolution period is established, so for the case of $\bar{t}_{s_1} = \bar{t}_{s_2} = 0.25$ and $\bar{t}_m = 1$, the total time considered is 1.5 dimensionless periods, with $N = 45$ and hence the number of design variables is 1035 and the number of nonlinear constraints is 838. The results corresponding to a transition maneuver between the steady-states associated to modulations $\overline{V}_{s_1} = 0.0$ and $\overline{V}_{s_2} = 0.5$ for different transition times are presented in Fig. 8. Variations in maneuver time around $\bar{t}_m = 3.0$ are considered. It can be observed, first, how the evolutions of the coning angle γ, shown in Fig. 8(a), significantly differ from the initial reference trajectories described in Eq. (31), defined by a ramp. Their evolution is mainly defined by the voltage modulation described in Fig. 8(d), which, given the weights described in Table 5, aims to ensure the tracking of steady-state conditions during the initial s_1 and final s_2 periods. Notably, the variation in maneuver time does not seem to affect the maximum values of $\overline{V}$ required to perform the optimal transition. Regarding the states that define the tether evolution in the plane, β, and the

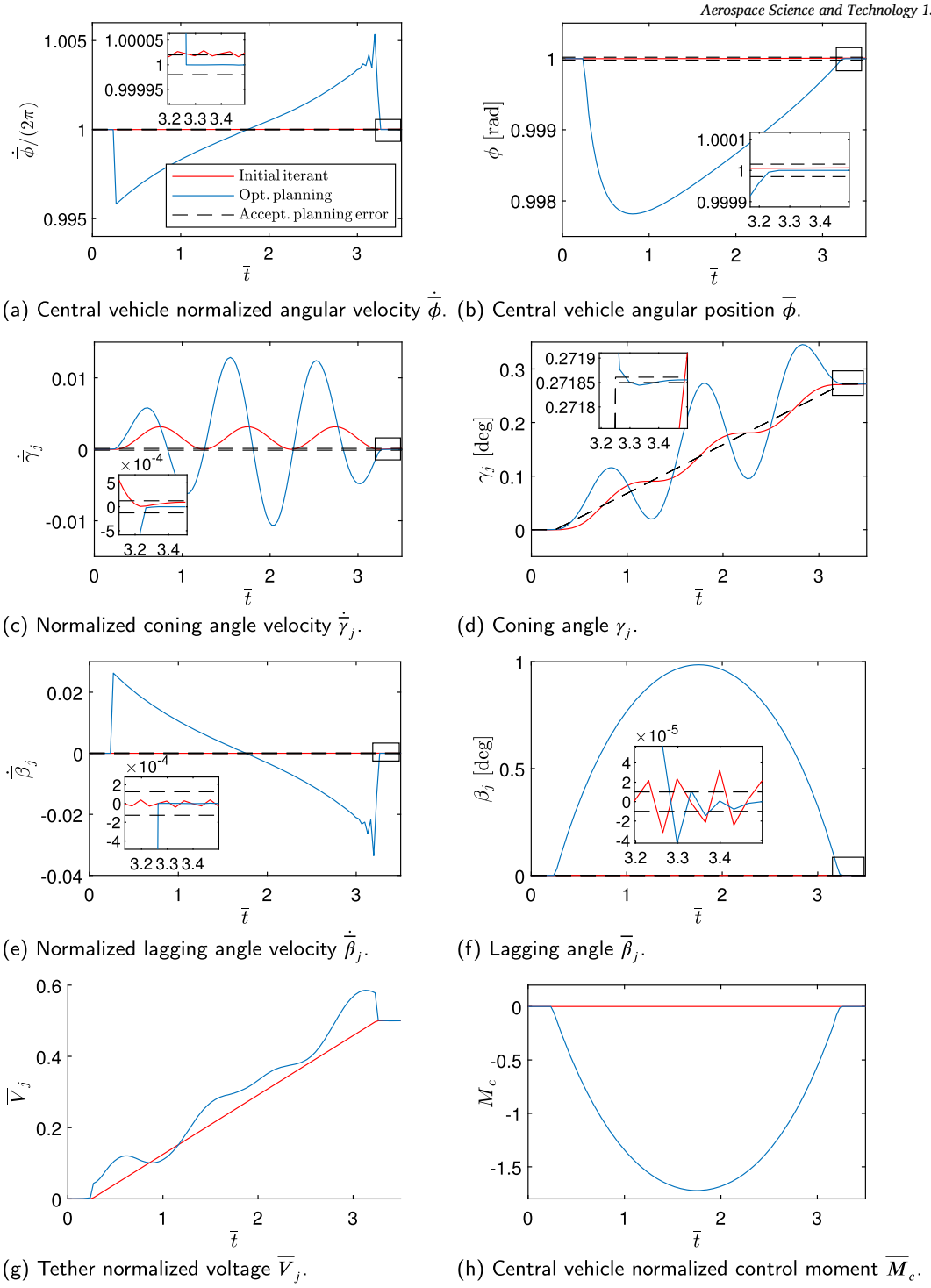

(a) Central vehicle normalized angular velocity $\dot{\bar{\phi}}$. (b) Central vehicle angular position $\bar{\phi}$.

(c) Normalized coning angle velocity $\dot{\bar{\gamma}}_j$. (d) Coning angle γ_j.

(e) Normalized lagging angle velocity $\dot{\bar{\beta}}_j$. (f) Lagging angle $\bar{\beta}_j$.

(g) Tether normalized voltage $\bar{V}_j$. (h) Central vehicle normalized control moment $\bar{M}_c$.

Fig. 7. Initial iterant and optimal solution for underactuated transition between $\bar{V}_{s_1} = 0.0$ and $\bar{V}_{s_2} = 0.2$ steady states considering $\bar{t}_m = 3.0$. (For interpretation of the colors in the figure(s), the reader is referred to the web version of this article.)

main vehicle's angular velocity, $\dot{\phi}$, Figs. 8(b) and (c) respectively show a more noticeable impact of the maneuver time $\bar{t}_m$. The oscillations of $\dot{\phi}$ around the nominal angular velocity, as well as those of the β angle relative to the radial direction, become more pronounced, in coherence with the greater control moment applied to the central vehicle. The results demonstrate the possibility of executing a transition maneuver between different steady-state points, which would be associated with different levels of thrust generated by the E-sail, while simultaneously controlling the relative angular positions of the tether with respect to the central vehicle, defined by γ and β, and the central vehicle's angular velocity. This indicates the control of an under-actuated system, as the use of $1 + p$ controls allows for determining the evolution of $1 + 2p$ states. Accepting the limitations of the model and the operational situation considered, this suggests the suitability of the proposed method for more detailed E-sail models with fewer simplifying assumptions.

Additionally, in Fig. 9 the impact of the change on the voltage modulation during the transition maneuver is studied. The evolution of states and controls for underactuated transition between an initial steady-state associated to $\bar{V}_{s_1} = 0.0$ to different final steady-state given by $\bar{V}_{s_2}$ are depicted.

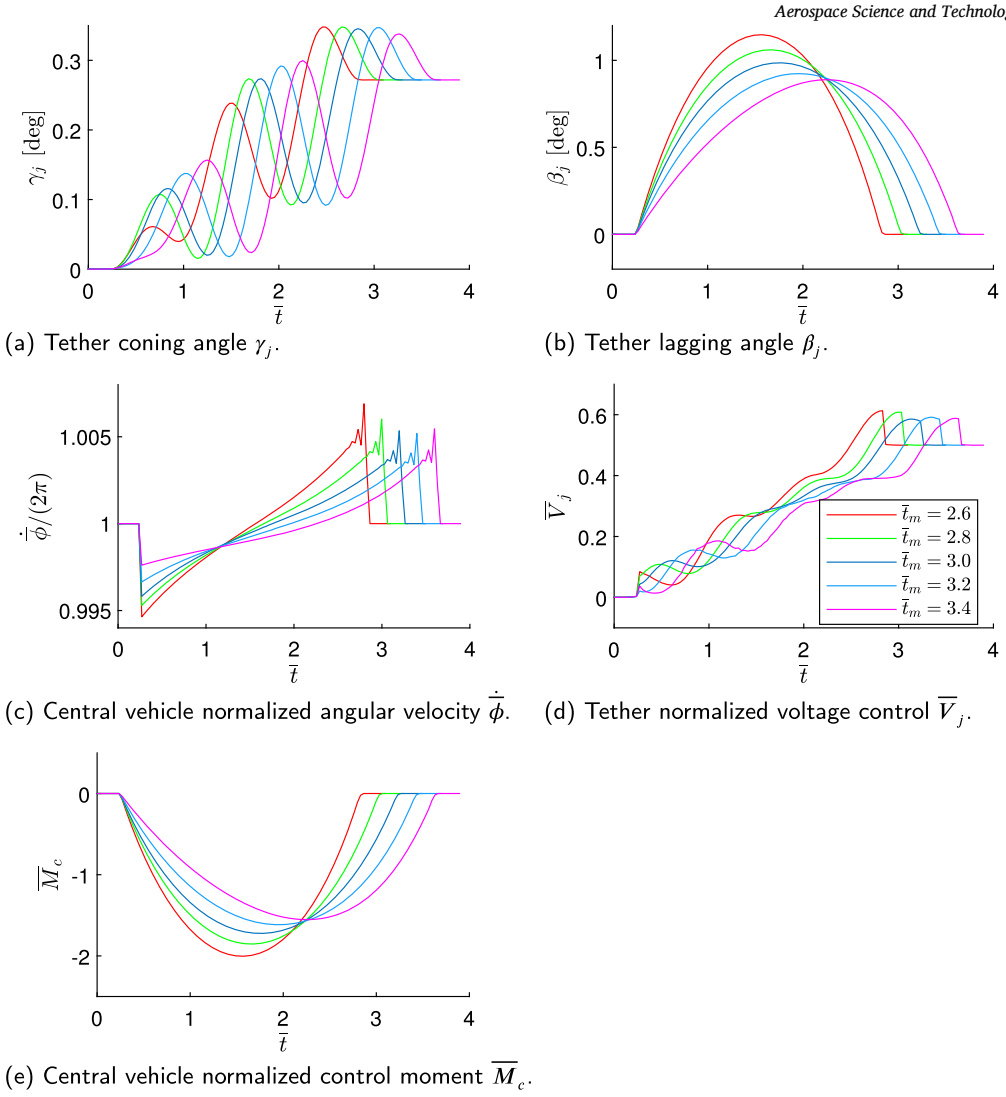

(a) Tether coning angle γ_j.
(b) Tether lagging angle β_j.
(c) Central vehicle normalized angular velocity $\dot{\bar{\phi}}$.
(d) Tether normalized voltage control $\overline{V}_j$.
(e) Central vehicle normalized control moment $\overline{M}_c$.

Fig. 8. Evolution of states and controls for underactuated transition between $\overline{V}_{s_1} = 0.0$ and $\overline{V}_{s_2} = 0.5$ steady states for different normalized transition times $\bar{t}_m$.

Results are provided for transition times $\bar{t}_m = 1.0$, 2.0, and 3.0, corresponding to durations of 1570, 3141, and 4712 seconds, respectively. First of all it should be observed that not all the transitions are possible for reduced transition intervals. For $\bar{t}_m = 1.0$ only transitioning from null voltage to 0.2 is possible. The possibility of transitioning to greater target voltage modulations is increased when a transition time equal to 2.0 is considered, but the direct transition to 1.0 remains unreachable. For a $\bar{t}_m = 3.0$, the full range of studied target voltage modulations given by $\overline{V}_{s_2} = 0.2$, 0.4, 0.6, 0.8 and 1.0 can be attained. In Fig. 9(d)-(e), the controls required to perform the maneuver between an initial state given by $\overline{V}_{s_1} = 0.0$ to a final value $\overline{V}_{s_2}$ for different values of the latter are shown. It is remarkable the increase on the required control moment to reach a certain $\overline{V}_{s_2}$ with the reduction of $\bar{t}_m$. Fig. 9(a)-(c) represent the evolution of the most representative states of the system. Results in Fig. 9(b) and (c) reveal a logical increase of the maximum perturbation in the angular spin and lagging angle, respectively, as the maneuver time is reduced.

Regarding the control requirements and their evolution, it can be observed in Fig. 9(d) that, first, given the chosen weights for the cost function, the evolution of the adimensional tethers' voltage $\overline{V}_j$ remains very close to the imposed ramp reference evolution, and in any case, a relatively smooth evolution is observed, except for the peak that appears during the transition to the arrival steady-state for some cases, which is attributed to the discretization considered. Similarly, for both the control moment $\overline{M}_c$, described in Fig. 9(e), the necessary evolution is very close to a sine signal, whose amplitude increase with the value of $\overline{V}_{s_2}$ and the reduction of the maneuver time. This behavior can be clearly observed in Fig. 10(a), which shows the maximum control torque requirements $\overline{M}_{c_{max}}$ for $\bar{t}_m = 2.0$ and 3.0. The marked impact observed suggests that the selected time for executing these maneuvers has a direct and significant impact on the choice of actuators needed to meet the control power requirements associated with these maneuvers.

4.2. Results for trajectory tracking

In this section, the results for the tracking of the optimal solution for the transition of an E-sail between two equilibrium states are presented. To validate the effectiveness of the proposed MPC against uncertainties in the solar wind evolution and representative random errors in the initial conditions, an analysis using the Monte Carlo method is presented. The behavior of the controlled system during the tracking of the optimal trajectory is evaluated by considering temporal evolutions of the solar wind at different distances from the Sun and angular positions in the plane of the ecliptic,

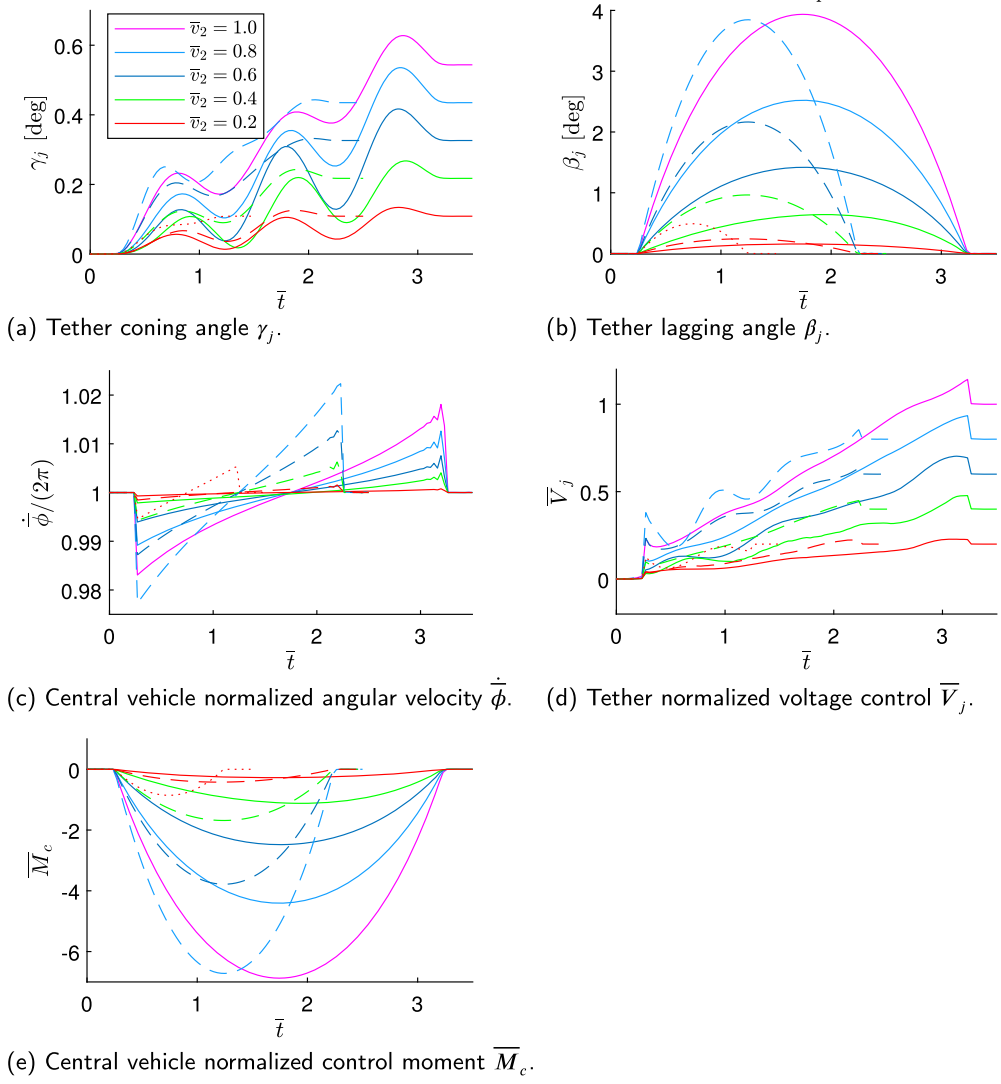

(a) Tether coning angle γ_j.

(b) Tether lagging angle β_j.

(c) Central vehicle normalized angular velocity $\dot{\phi}$.

(d) Tether normalized voltage control $\overline{V}_j$.

(e) Central vehicle normalized control moment $\overline{M}_c$.

Fig. 9. Evolution of states and controls for underactuated transition between $\overline{V}_{s_1} = 0.0$ and $\overline{V}_{s_2}$ steady-states. Transition times $\bar{t}_m = 1.0$ (dot), 2.0 (dash) and 3.0 (solid) are considered.

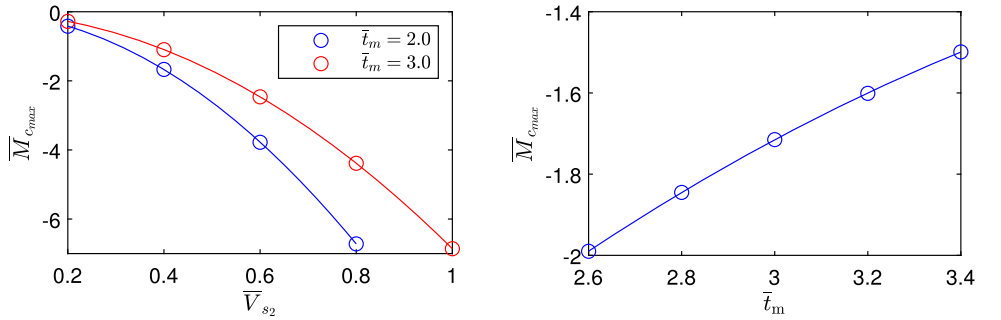

(a) Target steady-states given by $\overline{V}_{s_2}$, for transition times $\bar{t}_m = 2.0$ and 3.0.

(b) Target steady-state given by $\overline{V}_{s_2} = 0.5$, for normalized transition times $\bar{t}_m$.

Fig. 10. Evolution of maximum normalized control moment $\overline{M}_{c_{max}}$ for E-sail transition starting at $\overline{V}_{s_1} = 0.0$.

obtained from Enlil, and expressed in terms of the equivalent solar wind factor f_w, defined in Eq. (6). Additionally, the initial conditions contain, exclusively for angular position coordinates γ_j and β_j, random deviations from the nominal steady states, following a normal distribution with a mean of zero and a standard deviation twice the acceptable errors defined in Table 2.

As stated in Sect. 3.3, where the tracking problem using a SHMPC approach is introduced, the problem is solved using normalized constraint equations and design variables. The normalization factors for this objective are presented in Table 6. Similarly, the weights for the cost function are tailored according to the specifications provided in Table 7. Regarding the definition of the weights for the tracking phase compared to those for planning, shown in Table 5, it is worth highlighting the dominance of the weights associated with eliminating tether deviations, $\Lambda_{\Delta\gamma}$ and $\Lambda_{\Delta\beta}$, over

Table 6
Definition of normalization factors considered for SHMPC resolution.

Factor	$f_{\ddot{\phi}}$	$f_{\ddot{\gamma}}$	$f_{\ddot{\beta}}$	$f_{\dot{\phi}}$	$f_{\dot{\gamma}}$	$f_{\dot{\beta}}$	f_{ϕ}	f_{γ}	f_{β}	f_{M_c}	f_V
Value	10^{-3}	10^{-2}	10^{-3}	2π	10^{-2}	10^{-2}	2π	10^{-3}	10^{-3}	10^{-1}	10^{-1}

Table 7
Definition of the weight factor for the cost function for SHMPC resolution.

	$\Lambda_{\dot{\phi}}$	$\Lambda_{\dot{\gamma}}$	$\Lambda_{\dot{\beta}}$	Λ_{ϕ}	Λ_{γ}	Λ_{β}	$\Lambda_{\Delta\gamma}$	$\Lambda_{\Delta\beta}$	Σ_{M_c}	Σ_V
$k = 1, ..., N_p + 1$	1.00	0.01	0.01	1.00	50.00	50.00	70.00	2000.00	1.00	1.00

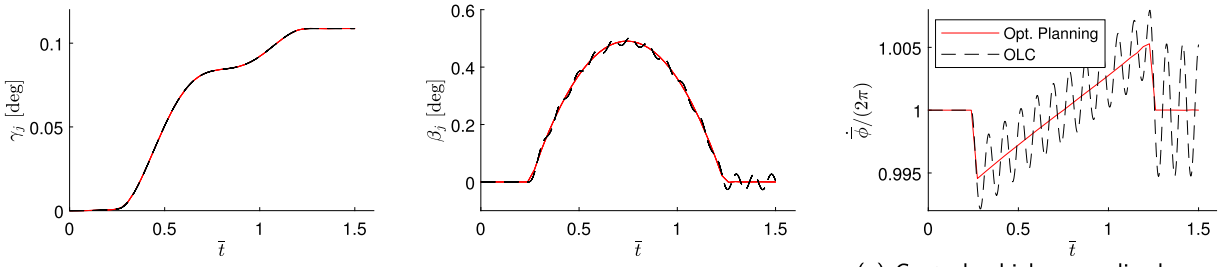

(a) Tether coning angle γ_j.

(b) Tether lagging angle β_j.

(c) Central vehicle normalized angular velocity $\dot{\bar{\phi}}$.

Fig. 11. Evolution of states and controls for optimal transition planning and system evolution under the open-loop control (OLC) law. The transition is defined between $\overline{V}_{s_1} = 0.0$ and $\overline{V}_{s_2} = 0.2$ for a transition time $\bar{t}_m = 1.0$.

those associated with angular positions, Λ_γ and Λ_β. Additionally, it should be noted that the weights for the controls, Σ_{M_c} and Σ_V, are substantially reduced, given that the objective in this phase is to ensure optimal trajectory tracking.

Finally, regarding additional adjustments for solving the optimization problem, the tolerance of the constraints is set to 10^{-6}, the optimality tolerance of the cost function is set to 10^{-4}, and the maximum number of iterations is set to 200. The MPC parameters considered are selected as a reasonable trade-off between accuracy and computational performance being $\overline{h} = 0.02$ and the control horizon N_c set to five. This selection is based on the system's natural frequencies and the results of a sensitivity analysis assessing the impact of $\overline{h}$ and N_c. The details of these analyses have not been included here for brevity. For the initial prediction horizon, which is the longest one and has a duration of $\overline{H}_p = 1.5$, the number of discretization points is $N_p + 1 = \overline{H}_p/\overline{h} + 1 = 76$. Hence, the maximum number of design variables for the OCP is computed as 1748. With regards to the time integration of the system dynamics, the *ode45* function in MATLAB R2023b is used. The RelTol and AbsTol parameters are both set to 10^{-10}, a choice verified to ensure convergence.

In the results presented in Fig. 11, the state and control evolutions are shown for the transition between $\overline{V}_{s_1} = 0.0$ to $\overline{V}_{s_2} = 0.2$ for a transition time $\bar{t}_m = 1.0$. The optimal planning solution presented in Sect. 4.1 is represented together with the system's evolution under the application of the open-loop optimal control law associated with the planning. For this result, average solar wind magnitudes and null initial deviation on tether positions are considered. It is important to note that the open-loop optimal control law uses linear interpolation to obtain the control law outside the discrete points where the planning problem's solution is obtained. This fact, among others, justifies the error in following the planned trajectory when applying the open-loop optimal control law for the transition problem, which is notably observed in Figs. 11(b) and (c). In the Fig. 12, the results provided for the same transition but applying the feedback law to the system and considering the initial deviation on tethers position and solar wind fluctuation, demonstrate the effectiveness of the RHMPC approach for effectively tracking the planned optimal trajectory. The state evolutions are represented alongside their corresponding admissible control errors. As shown in Figs. 12(a)-(d), it can be observed that the deviations in all the velocities and the angular position of the central vehicle remain within the imposed limits throughout the entire transition. In addition, with regard to the coning and lagging angles shown in Figs. 12(f) and (e), initial non-uniform deviations in the positions of the tethers can be seen. The voltage modulation displayed in Fig. 12(h), which is different for each tether, combined with the application of control moment described in Fig. 12(g), enables the system to reach the target steady-state conditions while satisfying the established control errors for all the tethers. This is achieved even in the presence of solar wind fluctuations, as shown in Fig. 12(i). Finally, in Fig. 13, the results of a Monte Carlo analysis are presented for the transition between $\overline{V}_{s_1} = 0.0$ to $\overline{V}_{s_2} = 0.2$ for a $\bar{t}_m = 1.0$, considering 200 cases of non-homogeneous initial deviations in the angular positions of the tethers and solar wind fluctuations obtained for Enlil [74] and represented in Fig. 13(i). The representation of the average values and standard deviations demonstrates the effectiveness of the proposed Receding Horizon Model Predictive Control (RHMPC) for executing the transition maneuver. The RHMPC successfully achieves the target steady-state while meeting acceptable error limits, and it effectively reduces the initial deviations in γ, as shown in Fig. 13(e). In the case of deviations in β between tethers, as depicted in Fig. 13(f), the procedure is somewhat less efficient, though it still maintains deviations within acceptable error bounds. Table 8 presents, the mean values m_x and standard deviations σ_x for the coning angles $x = \gamma$ and lagging angles $x = \beta$ at the initial and final moments of the transition. The results are provided in degrees. It can be observed that the mean of the coning angle shifts from being close to zero to a value closer to $\gamma_{s_2} \approx 0.1$, which according to Fig. 4(a) corresponds to the coning angle associated to the steady state operation for $\overline{V}_{s_2} = 0.2$. Additionally, the standard deviation σ_γ decreases, which quantitatively demonstrates the effectiveness of

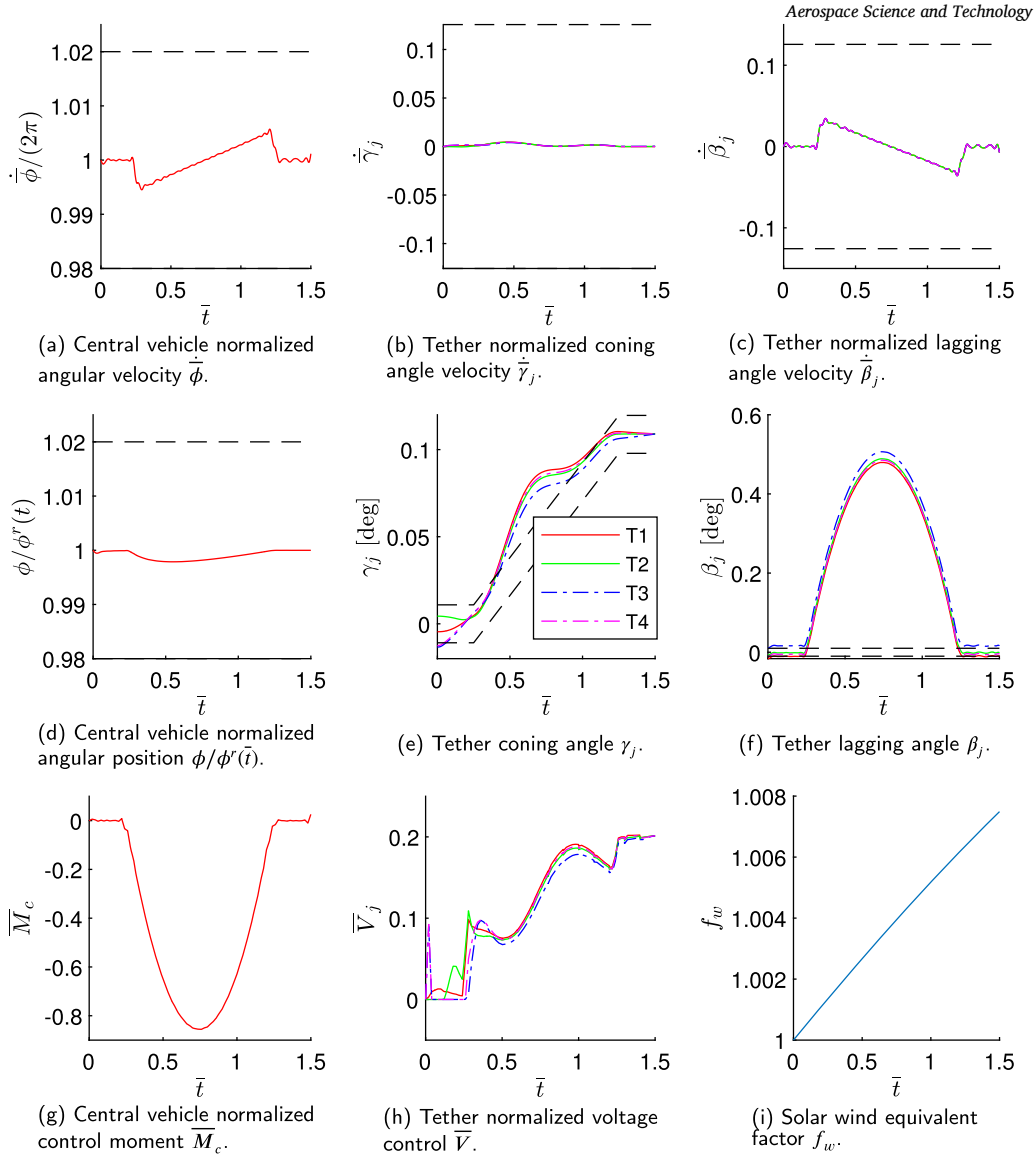

Fig. 12. Evolution of states and controls for underactuated tracking of optimal transition between an steady-states associated to $\overline{V}_{s_1} = 0.0$ and $\overline{V}_{s_2} = 0.2$ for a transition time $\bar{t}_m = 1.0$.

Table 8
Summary of MC results for SHMPC for E-sail optimal transition between an steady-state $\overline{V}_{s_1} = 0.0$ to $\overline{V}_{s_2} = 0.2$ for a transition time $\bar{t}_m = 1.0$.

$\bar{t}$	γ		β	
	$m_\gamma - \gamma_{s_2}$ [°]	σ_γ [°]	m_β [°]	σ_β [°]
$\bar{t}_i$	0.0003	0.0107	0.00004	0.0116
$\bar{t}_f$	0.0003	0.0005	-0.0001	0.0097

the proposed control procedure. On the other hand, an analysis of the mean and standard deviation of the lagging angle β confirms a more moderate reduction in the standard deviation but a slight worsening of the mean, which is ideally zero degrees at both the initial and final moments.

5. Conclusions and future works

Under the described hypotheses and assumptions, this article validates the feasibility of executing stable transitions between two steady-state conditions of an E-sail, using only voltage modulation and control torque applied to the central vehicle. This result suggests the potential for

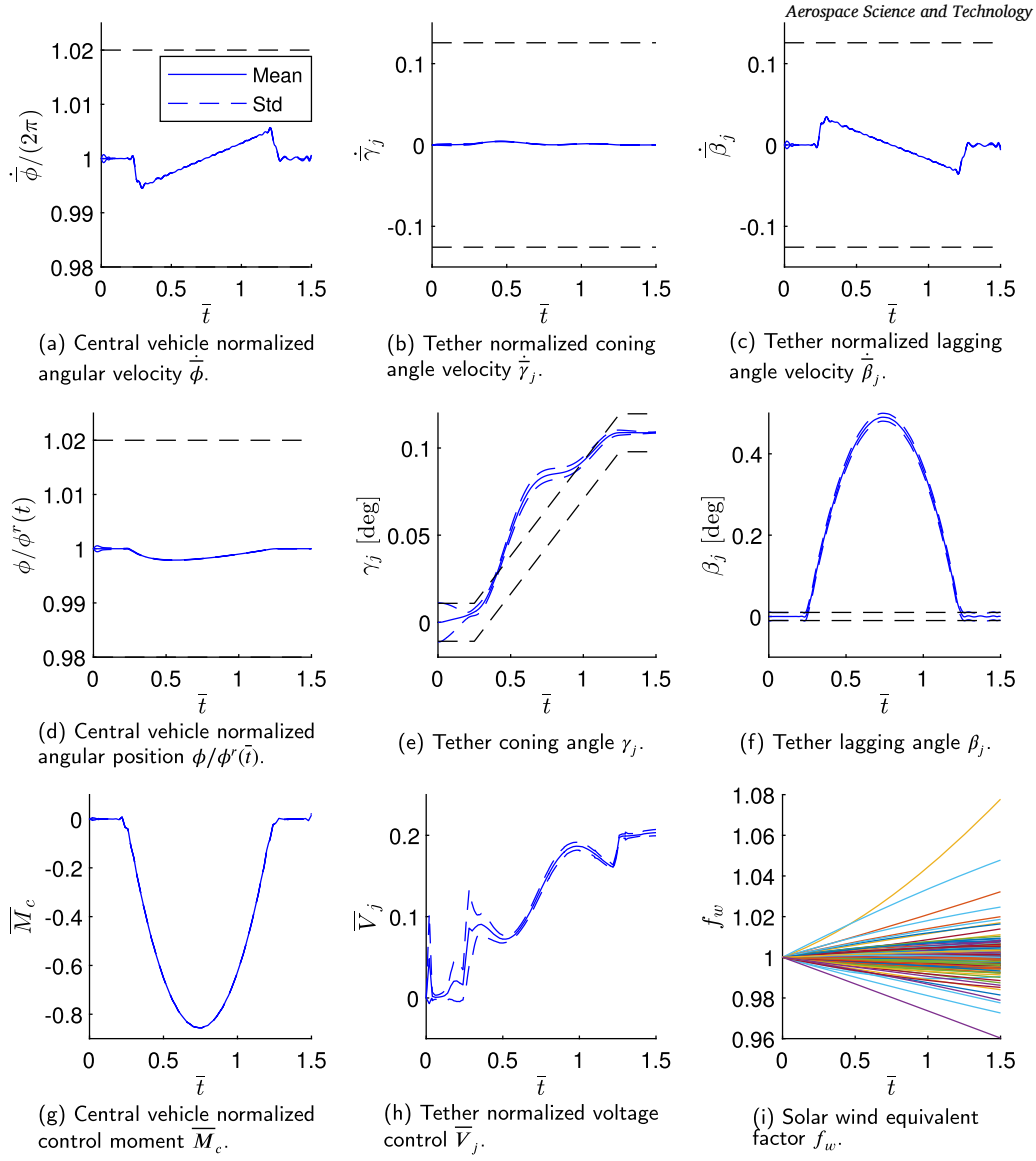

(a) Central vehicle normalized angular velocity $\dot{\bar{\phi}}$.
(b) Tether normalized coning angle velocity $\dot{\bar{\gamma}}_j$.
(c) Tether normalized lagging angle velocity $\dot{\bar{\beta}}_j$.
(d) Central vehicle normalized angular position $\phi/\phi^r(\bar{t})$.
(e) Tether coning angle γ_j.
(f) Tether lagging angle β_j.
(g) Central vehicle normalized control moment $\overline{M}_c$.
(h) Tether normalized voltage control $\overline{V}_j$.
(i) Solar wind equivalent factor f_w.

Fig. 13. Results of Monte Carlo analysis for under-actuated tracking of optimal transition between an steady-state $\overline{V}_{s_1} = 0.0$ to $\overline{V}_{s_2} = 0.2$ for a transition time $\bar{t}_m = 1.0$. Realistic solar pressure and random deviations on initial conditions have been considered for 200 scenarios. The evolution of mean and standard deviation of the states and controls is provided.

controlling an E-sail without secondary tethers, modeled from a multibody perspective and without applying forces to remote units. This approach would significantly simplify the system architecture and further emphasize its propellantless nature.

Regarding transition planning, this study demonstrates the effectiveness of formulating the inversion problem as an optimal control problem using a simplified model described by Ordinary Differential Equations (ODEs). The calculated control requirements for executing optimal transitions between steady states reveal the influence of maneuver duration and voltage increment, with shorter transition times and larger voltage changes leading to higher control demands. For a transition period of $\bar{t}_m = 1.0$, convergence was achieved only for a moderate voltage increment, up to $\overline{V}_{s_2} = 0.2$. However, extending the transition time to $\bar{t}_m = 2.0$ and 3.0 allowed for larger transitions, reaching $\overline{V}_{s_2} = 0.8$ and $\overline{V}_{s_2} = 1.0$, respectively. These results provide valuable insights for sizing the control system's capabilities and defining the operational envelope.

In addition, a Monte Carlo analysis confirms that tracking the reference trajectory is feasible under the assumptions of the simplified model, even in the presence of realistic solar wind perturbations and non-homogeneous initial deviations in the tether positions, using a nonlinear shrinking MPC scheme. The proposed inversion and tracking methods provide satisfactory results in both phases, enabling efficient planning and precise tracking. Furthermore, given their flexibility, ease of implementation in more detailed models—including those formulated as DAEs—and their capacity to handle uncertainties and perturbations, the findings of this study encourage the application of these methodologies to more detailed E-sail models, particularly those incorporating flexible elements, and to more general operating scenarios.

In future works, the extension of the findings of this research should be addressed. First, while control strategies have been studied under zero sailing angle conditions, future research should investigate the application of these methods for non-zero sailing angles, as indicated by existing trajectory planning studies. Additionally, stable transitions between operations at different sailing angles should be explored. Robust control strategies must be developed to ensure system stability and performance under uncertainties in solar wind parameters and external disturbances. The Monte Carlo method used in this research for robustness evaluation should be expanded by incorporating more advanced robust control schemes. Finally, although this work has primarily focused on control strategies, the state estimation problem requires further investigation. Integrating state estimation

into control assessments would provide a more comprehensive evaluation of system performance, beyond the current approach based on admissible measurement errors.

CRediT authorship contribution statement

Guillermo Pacheco-Ramos: Writing – review & editing, Writing – original draft, Validation, Software, Methodology, Conceptualization. **Rafael Vazquez:** Writing – review & editing, Validation, Methodology, Conceptualization. **Daniel Garcia-Vallejo:** Writing – review & editing, Validation, Methodology, Conceptualization.

Declaration of generative AI and AI-assisted technologies in the writing process

The authors would like to acknowledge the use of ChatGPT by OpenAI for language improvement in the preparation of this manuscript. After using this tool, the authors reviewed and edited the content as needed and take full responsibility for the content of the publication.

Declaration of competing interest

The authors declare that they have no known competing financial interests or personal relationships that could have appeared to influence the work reported in this paper.

Acknowledgements

Guillermo Pacheco-Ramos and Rafael Vazquez acknowledge support of grant PID2023-147623OB-I00 funded by MICIU/AEI/10.13039/501100011033 and by "ERDF A way of making Europe".

Appendix A. Formulation of simplified model

This annex describes the detailed description of the calculation of the kinetic energy of the E-sail.

A.1. Kinetic energy

Given the expression for the kinetic energy of the system in Eq. (2), the kinetic energy of the central body, considering the linear and angular terms is

$$T_r = \frac{1}{2} m_r \dot{r}^2 + \frac{1}{2} I_r \dot{\phi}^2, \tag{43}$$

being m_r the mass of the central vehicle and I_r its moment of inertia around the X_B axis. The contribution of the tether j, can be expressed as the integral of the contribution of the local velocity as

$$T_{t_j} = \int_0^{L_t} \frac{1}{2} \rho_t A_t \left(\dot{\mathbf{r}}_{xI}^I\right)^\top \dot{\mathbf{r}}_{xI}^I \mathrm{dx}, \tag{44}$$

where A_t is the cross section area of the tether, ρ_t its mass density and $\dot{\mathbf{r}}_{xI}^I$ represents the absolute velocity of a point x of the tether, expressed on the inertial coordinate system. The expression for the relative velocity of a point on the tether with respect to the origin of the G system, expressed in the G system, is defined as

$$\left.\frac{d\mathbf{r}_{xs}}{dt}\right)_G^G = C_N^G \left(\boldsymbol{\omega}_{N/G}\right)^\times \mathbf{r}_{xG}, \tag{45}$$

where $()^\times$ represents the matrix expression of the cross product, C_t^s represents the rotation matrix from frame N to G, which is a function of the coning angle γ as

$$C_N^G = \begin{bmatrix} \cos(\gamma) & \sin(\gamma) & 0 \\ -\sin(\gamma) & \cos(\gamma) & 0 \\ 0 & 0 & 1 \end{bmatrix} \tag{46}$$

$\boldsymbol{\omega}_{N/G}$ is the angular velocity of frame N with respect to G, expressed in N, and is equal to $\boldsymbol{\omega}_{N/G} = \begin{bmatrix} 0 & 0 & -\dot{\gamma} \end{bmatrix}^\top$. Finally, $\mathbf{r}_{xG}$ represents the position of a point on the tether with respect to the origin of frame G, expressed in frame N, being $\mathbf{r}_{xG} = \begin{bmatrix} 0 & x & 0 \end{bmatrix}^\top$.

The expression of the velocity of a point of the tether respect to Z, expressed in Z frame, is given by

$$\left.\frac{d\mathbf{r}_{xZ}}{dt}\right)_Z^Z = C_G^Z \left.\frac{d\mathbf{r}_{xG}}{dt}\right)_G^G + C_G^Z \left(\boldsymbol{\omega}_{G/Z}^G\right)^\times C_N^G \mathbf{r}_{xG}^\top, \tag{47}$$

where the fact that the origins of the reference frames G and z coincide has been considered. The angular velocity and transformation matrix are defined as $\boldsymbol{\omega}_{G/Z}^s = \begin{bmatrix} \dot{\beta} & 0 & 0 \end{bmatrix}^\top$ and

$$C_G^Z = \begin{bmatrix} 1 & 0 & 0 \\ 0 & \cos(\beta) & -\sin(\beta) \\ 0 & \sin(\beta) & \cos(\beta) \end{bmatrix}, \tag{48}$$

respectively, being β the lagging angle. Similarly, the velocity respect to the body frame, is calculated as

$$\left.\frac{d\mathbf{r}_{xB}}{dt}\right)_B^B = C_Z^B \left.\frac{d\mathbf{r}_{xZ}}{dt}\right)_Z^Z, \tag{49}$$

where the fact that the angle ζ is constant has been considered, and the transformation matrix C_Z^B is defined as

$$C_Z^B = \begin{bmatrix} 1 & 0 & 0 \\ 0 & \cos(\zeta) & -\sin(\zeta) \\ 0 & \sin(\zeta) & \cos(\zeta) \end{bmatrix}. \tag{50}$$

To conclude the angular velocity composition, the velocity of a tether point respect to the origin of R frame is given by

$$\left.\frac{d\mathbf{r}_{xR}}{dt}\right)_R^R = C_B^R \left.\frac{d\mathbf{r}_{xB}}{dt}\right)_B^B + C_B^R \left(\boldsymbol{\omega}_{B/R}^B\right)^\times \mathbf{r}_{xB}^B, \tag{51}$$

where the position of the point respect to B expressed in B is given by

$$\mathbf{r}_{xB}^B = C_Z^B \left(\mathbf{r}_{ZB}^Z + C_s^Z C_t^s \mathbf{r}_{xs}^\top\right), \tag{52}$$

being $\mathbf{r}_{ZB}^Z = \begin{bmatrix} 0 & R_r & 0 \end{bmatrix}^\top$, and C_B^R

$$C_B^R = \begin{bmatrix} 1 & 0 & 0 \\ 0 & \cos(\phi) & -\sin(\phi) \\ 0 & \sin(\phi) & \cos(\phi) \end{bmatrix}, \tag{53}$$

where ϕ is the angular position of the Y_B axis respect to Y_R. Finally, the total velocity respect to the inertial frame H is computed by adding the velocity of the main vehicle along X_H, defined as $\left.\frac{d\mathbf{r}_{RH}}{dt}\right)_H^H = \begin{bmatrix} \dot{r} & 0 & 0 \end{bmatrix}^\top$, resulting in

$$\left.\frac{d\mathbf{r}_{xH}}{dt}\right)_H^H = \left.\frac{d\mathbf{r}_{xR}}{dt}\right)_R^R + \left.\frac{d\mathbf{r}_{RH}}{dt}\right)_H^H, \tag{54}$$

here, it has been considered the fact that frames R and H are parallel, leading to $\left.\frac{d\mathbf{r}_{xR}}{dt}\right)_H^H = \left.\frac{d\mathbf{r}_{xR}}{dt}\right)_R^R$.

Taking into account the formulation details provided in Eq. (45) to (54) and integrating Eq. (44), the kinetic energy of the j-th tether can be expressed in terms of the generalized coordinates and its time derivatives as

$$\begin{aligned} T_{t_j} = &\left(\frac{m_t R_r^2}{2} + \frac{L_t m_t \cos(\beta_j) R_r \cos(\gamma_j)}{2} + \frac{J_t \cos(\gamma_j)^2}{2}\right)\dot{\phi}^2 + \frac{J_t}{2}\dot{\gamma}_j^2 \\ &+ \frac{J_t \cos(\gamma_j)^2}{2}\dot{\beta}_j^2 + \frac{m_t \dot{r}^2}{2} + \frac{L_t m_t \dot{\gamma}_j \dot{r} \cos(\gamma_j)}{2} \\ &+ \left(J_t \cos(\gamma_j)^2 + \frac{L_t m_t R_r \cos(\beta_j)\cos(\gamma_j)}{2}\right)\dot{\beta}_j \dot{\phi} - \frac{L_t m_t R_r \dot{\gamma}_j \dot{\phi} \sin(\beta_j)\sin(\gamma_j)}{2}, \end{aligned} \tag{55}$$

where $J_t = 1/3\, m_t L_t^2$. In regards to the kinetic energy of the remote units, it is computed similarly to the calculation defined for the tethers. The particularization of Eq. (44) for point masses of value m_u located at the tip of the tethers ($x = L$) leads to

$$\begin{aligned} T_{u_j} = &\left(\frac{m_u R_r^2}{2} + L_t m_u \cos(\beta_j) R_r \cos(\gamma_j) + \frac{I_u \cos(\gamma_j)^2}{2}\right)\dot{\phi}^2 + \frac{I_u}{2}\dot{\gamma}_j^2 \\ &+ \frac{I_u \cos(\gamma_j)^2}{2}\dot{\beta}_j^2 + \frac{m_u \dot{r}^2}{2} + L_t m_u \dot{\gamma}_j \dot{r} \cos(\gamma_j) - L_t m_u R_r \dot{\gamma}_j \dot{\phi} \sin(\beta_j)\sin(\gamma_j) \\ &+ \left(I_u \cos(\gamma_j)^2 + L_t m_u R_r \cos(\beta_j)\cos(\gamma_j)\right)\dot{\beta}_j \dot{\phi}, \end{aligned} \tag{56}$$

where $I_u = m_u L_t^2$ represents the remote mass inertia respect to the anchor point.

The application of velocity composition recursively allows for the calculation of the absolute velocity of each point on the tether, as described below.

Data availability

Data will be made available on request.

References

[1] P. Janhunen, Electric sail for spacecraft propulsion, J. Propuls. Power 20 (2004) 763–764, https://doi.org/10.2514/1.8580.
[2] P. Janhunen, The electric sail - a new propulsion method which may enable fast missions to the outer solar system, JBIS, J. Br. Interplanet. Soc. 61 (8) (2008) 322–325.
[3] M. Bassetto, L. Niccolai, A.A. Quarta, G. Mengali, A comprehensive review of electric solar wind sail concept and its applications, Prog. Aerosp. Sci. 128 (September 2021) 100768, https://doi.org/10.1016/j.paerosci.2021.100768.

[4] G. Mengali, A.A. Quarta, Non-Keplerian orbits for electric sails, Celest. Mech. Dyn. Astron. 105 (1) (2009) 179–195, https://doi.org/10.1007/s10569-009-9200-y.
[5] J. Urrios, G. Pacheco-Ramos, R. Vazquez, Optimal planning and guidance for solar system exploration using electric solar wind sails, Acta Astronaut. 217 (2024) 116–129, https://doi.org/10.1016/j.actaastro.2024.01.030.
[6] P.K. Toivanen, P. Janhunen, Spin plane control and thrust vectoring of electric solar wind sail, J. Propuls. Power 29 (2013) 178–185, https://doi.org/10.2514/1.B34330.
[7] P. Toivanen, P. Janhunen, Electric Solar Wind Sail: Deployment, Long-Term Dynamics, and Control Hardware Requirements, Springer Berlin Heidelberg, Berlin, Heidelberg, 2014, pp. 977–987.
[8] P. Janhunen, P. Toivanen, TI tether rig for solving secular spinrate change problem of electric sail, https://doi.org/10.48550/arXiv.1603.05563, 2016.
[9] G. Pacheco-Ramos, D. Garcia-Vallejo, R. Vazquez, Formulation of a high-fidelity multibody dynamical model for an electric solar wind sail, Int. J. Mech. Sci. 256 (2023) 108466, https://doi.org/10.1016/j.ijmecsci.2023.108466.
[10] P. Janhunen, A.A. Quarta, G. Mengali, Electric solar wind sail mass budget model, Geosci. Instrum. Method. Data Syst. 2 (2013) 85–95, https://doi.org/10.5194/gi-2-85-2013.
[11] C. Du, Z.H. Zhu, Dynamic characterization and sail angle control of electric solar wind sail by high-fidelity tether dynamics, Acta Astronaut. 189 (2021) 504–513, https://doi.org/10.1016/j.actaastro.2021.09.019.
[12] J. Kang, K.-C. Park, Flexible heliogyro solar sail under solar radiation pressure and gravitational force, Acta Astronaut. 179 (2021) 186–196, https://doi.org/10.1016/j.actaastro.2020.10.042.
[13] M. Bassetto, A.A. Quarta, A. Caruso, G. Mengali, Optimal heliocentric transfers of a sun-facing heliogyro, Aerosp. Sci. Technol. 119 (2021), https://doi.org/10.1016/j.ast.2021.107094.
[14] P. Janhunen, Photonic spin control for solar wind electric sail, Acta Astronaut. 83 (2013) 85–90, https://doi.org/10.1016/j.actaastro.2012.10.017.
[15] P. Janhunen, Electric sail, photonic sail and deorbiting applications of the freely guided photonic blade, Acta Astronaut. 93 (2014) 410–417, https://doi.org/10.1016/j.actaastro.2013.07.041.
[16] P. Janhunen, P. Toivanen, An intrinsic way to control e-sail spin, https://doi.org/10.48550/ARXIV.1406.6847, 2014.
[17] P. Toivanen, P. Janhunen, J. Envall, Electric sail control mode for amplified transverse thrust, Acta Astronaut. 106 (2015) 111–119, https://doi.org/10.1016/j.actaastro.2014.10.031.
[18] P. Toivanen, P. Janhunen, Thrust vectoring of an electric solar wind sail with a realistic sail shape, Acta Astronaut. 131 (2017) 145–151, https://doi.org/10.1016/j.actaastro.2016.11.027.
[19] M. Bassetto, G. Mengali, A.A. Quarta, Thrust and torque vector characteristics of axially-symmetric E-sail, Acta Astronaut. 146 (2018) 134–143, https://doi.org/10.1016/j.actaastro.2018.02.035.
[20] M. Bassetto, G. Mengali, A.A. Quarta, Attitude dynamics of an electric sail model with a realistic shape, Acta Astronaut. 159 (2019) 250–257, https://doi.org/10.1016/j.actaastro.2019.03.064.
[21] M. Bassetto, G. Mengali, A.A. Quarta, E-sail attitude control with tether voltage modulation, Acta Astronaut. 166 (2020) 350–357, https://doi.org/10.1016/j.actaastro.2019.10.023.
[22] F. Liu, Q. Hu, J. Zhang, K. Yang, Y. Li, Dynamics of single charged wire for solar wind electric sail dynamics of single charged wire for solar wind electric sail, in: 31st International Symposium on Space Technology and Sciences, Japan Soc. for Aeronautical and Space Sciences Paper 2017-o-1-05, Tokyo, Japan, 2017.
[23] G.Q. Li, Z.H. Zhu, Long-term dynamic modeling of tethered spacecraft using nodal position finite element method and symplectic integration, Celest. Mech. Dyn. Astron. 123 (2015) 363–386, https://doi.org/10.1007/s10569-015-9640-5.
[24] G. Li, Z.H. Zhu, C. Du, S.A. Meguid, Characteristics of coupled orbital-attitude dynamics of flexible electric solar wind sail, Acta Astronaut. 159 (2019) 593–608, https://doi.org/10.1016/j.actaastro.2019.02.009.
[25] G. Li, Z.H. Zhu, C. Du, Flight dynamics and control strategy of electric solar wind sails, J. Guid. Control Dyn. 43 (2020) 462–474, https://doi.org/10.2514/1.G004608.
[26] C. Du, Z.H. Zhu, G. Li, Rigid-flexible coupling effect on attitude dynamics of electric solar wind sail, Commun. Nonlinear Sci. Numer. Simul. 95 (2021) 105663, https://doi.org/10.1016/j.cnsns.2020.105663.
[27] C. Du, Z.H. Zhu, G. Li, Analysis of thrust-induced sail plane coning and attitude motion of electric sail, Acta Astronaut. 178 (2021) 129–142, https://doi.org/10.1016/j.actaastro.2020.09.001.
[28] C. Zhao, M. Huo, J. Qi, S. Cao, D. Zhu, L. Sun, H. Sun, N. Qi, Coupled attitude-vibration analysis of an E-sail using absolute nodal coordinate formulation, Astrodynamics 4 (2020) 249–263, https://doi.org/10.1007/s42064-020-0081-x.
[29] R. Wang, C. Wei, Y. Wu, Y. Zhao, The study of spin control of flexible electric sail using the absolute nodal coordinate formulation, in: 2017 IEEE International Conference on Cybernetics and Intelligent Systems (CIS) and IEEE Conference on Robotics, Automation and Mechatronics (RAM), 2017, pp. 785–790.
[30] H. Ren, T. Yuan, M. Huo, C. Zhao, S. Zeng, Dynamics and control of a full-scale flexible electric solar wind sail spacecraft, Aerosp. Sci. Technol. 119 (2021) 107087, https://doi.org/10.1016/j.ast.2021.107087.
[31] J.A. Fulton, H. Schaub, Fixed-axis electric sail deployment dynamics analysis using hub-mounted momentum control, Acta Astronaut. 144 (2018) 160–170, https://doi.org/10.1016/j.actaastro.2017.11.048.
[32] C. Du, Z.H. Zhu, J. Kang, Attitude control and stability analysis of electric sail, IEEE Trans. Aerosp. Electron. Syst. 58 (6) (2022) 5560–5570, https://doi.org/10.1109/TAES.2022.3175166.
[33] S. Zeng, W. Fan, H. Ren, An orbital-attitude coupled control framework for a full-scale flexible electric solar wind sail spacecraft in orbital transformation missions, Aerosp. Sci. Technol. 155 (2024) 109655, https://doi.org/10.1016/j.ast.2024.109655.
[34] Z. Meng, B. Wang, P. Huang, MPC-based anti-sway control of tethered space robots, Acta Astronaut. 152 (2018) 146–162, https://doi.org/10.1016/j.actaastro.2018.07.050.
[35] C.Q. Luo, J.L. Sun, H. Wen, D.P. Jin, Dynamics of a tethered satellite formation for space exploration modeled via ANCF, Acta Astronaut. 177 (2020) 882–890, https://doi.org/10.1016/j.actaastro.2019.11.028.
[36] L. Huang, H. Wen, L. Cheng, S. Xu, Nonlinear model predictive control for attitude maneuver of a barbell electric sail through voltage regulation, Acta Astronaut. 179 (2021) 146–152, https://doi.org/10.1016/j.actaastro.2020.10.028.
[37] G. Li, Z. Zhu, Model predictive control for electrodynamic tether geometric profile in orbital maneuvering with finite element state estimator, Nonlinear Dyn. 106 (2021) 473–489, https://doi.org/10.1007/s11071-021-06869-3.
[38] L. Chenguang, W. Wei, W. Changqing, Z. Ying, Deployment trajectory tracking control of tethered satellite system based on fast model predictive control, in: 2018 IEEE CSAA Guidance, Navigation and Control Conference (CGNCC), 2018, pp. 1–7.
[39] X. Li, G. Sun, Z. Kuang, S. Han, Nonlinear predictive optimization for deploying space tethered satellite via discrete-time fractional-order sliding mode, IEEE Trans. Aerosp. Electron. Syst. 58 (5) (2022) 4517–4526, https://doi.org/10.1109/TAES.2022.3166061.
[40] H. Wen, Z.H. Zhu, D. Jin, H. Hu, Model predictive control with output feedback for a deorbiting electrodynamic tether system, J. Guid. Control Dyn. 39 (10) (2016) 2455–2460, https://doi.org/10.2514/1.G000535.
[41] E.N. Hartley, A tutorial on model predictive control for spacecraft rendezvous, in: 2015 European Control Conference (ECC), 2015, pp. 1355–1361.
[42] A. Weiss, M. Baldwin, R.S. Erwin, I. Kolmanovsky, Model predictive control for spacecraft rendezvous and docking: strategies for handling constraints and case studies, IEEE Trans. Control Syst. Technol. 23 (4) (2015) 1638–1647, https://doi.org/10.1109/TCST.2014.2379639.
[43] G. Bucchioni, F. Alfino, M. Pagone, C. Novara, A minimum-propellant Pontryagin-based nonlinear mpc for spacecraft rendezvous in lunar orbit, in: 2023 62nd IEEE Conference on Decision and Control (CDC), 2023, pp. 8745–8750.
[44] J.C. Sanchez, F. Gavilan, R. Vazquez, Chance-constrained model predictive control for near rectilinear halo orbit spacecraft rendezvous, Aerosp. Sci. Technol. 100 (2020) 105827, https://doi.org/10.1016/j.ast.2020.105827.
[45] J.C. Sanchez, F. Gavilan, R. Vazquez, C. Louembet, A flatness-based predictive controller for six-degrees of freedom spacecraft rendezvous, Acta Astronaut. 167 (2020) 391–403, https://doi.org/10.1016/j.actaastro.2019.11.026.
[46] A. Guiggiani, I. Kolmanovsky, P. Patrinos, A. Bemporad, Fixed-point constrained model predictive control of spacecraft attitude, in: 2015 American Control Conference (ACC), 2015, pp. 2317–2322.
[47] S. Ahmed, E.C. Kerrigan, Suboptimal predictive control for satellite detumbling, J. Guid. Control Dyn. 37 (3) (2014) 850–859, https://doi.org/10.2514/1.61367.
[48] M. Mirshams, M. Khosrojerdi, Attitude control of an underactuated spacecraft using quaternion feedback regulator and tube-based mpc, Acta Astronaut. 132 (2017) 143–149, https://doi.org/10.1016/j.actaastro.2016.11.033.
[49] F. Bayat, Model predictive sliding control for finite-time three-axis spacecraft attitude tracking, IEEE Trans. Ind. Electron. 66 (10) (2019) 7986–7996, https://doi.org/10.1109/TIE.2018.2881936.

[50] A.D. Hayes, R.J. Caverly, Model predictive tracking of spacecraft deorbit trajectories using drag modulation, Acta Astronaut. 202 (2023) 670–685, https://doi.org/10.1016/j.actaastro.2022.10.057.
[51] D. García-Vallejo, J.L. Escalona, J. Mayo, J. Domínguez, Describing rigid-flexible multibody systems using absolute coordinates, Nonlinear Dyn. 34 (2003) 75–94, https://doi.org/10.1023/B:NODY.0000014553.98731.8d.
[52] P. Janhunen, A. Sandroos, Simulation study of solar wind push on a charged wire: basis of solar wind electric sail propulsion, Ann. Geophys. 25 (2007) 755–767, https://doi.org/10.5194/angeo-25-755-2007.
[53] P. Janhunen, PIC simulation of electric sail with explicit trapped electron modeling, ASP Conf. Ser. 459 (2012) 271–276.
[54] A. Sanchez-Torres, Propulsive force in an electric solar sail, Contrib. Plasma Phys. 54 (2014) 314–319, https://doi.org/10.1002/ctpp.201410077.
[55] P. Janhunen, Boltzmann electron PIC simulation of the E-sail effect, Ann. Geophys. 33 (2015) 1507–1512, https://doi.org/10.5194/angeo-33-1507-2015.
[56] B.M. Wiegmann, A. Heaton, Summary of NASA's electric sail propulsion investigations 2014-2017, in: AIAA Aerospace Sciences Meeting, 2018.
[57] P. Janhunen, P.K. Toivanen, J. Polkko, S. Merikallio, P. Salminen, E. Haeggström, H. Seppänen, R. Kurppa, J. Ukkonen, S. Kiprich, G. Thornell, H. Kratz, L. Richter, O. Krömer, R. Rosta, M. Noorma, J. Envall, S. Lätt, G. Mengali, A.A. Quarta, H. Koivisto, O. Tarvainen, T. Kalvas, J. Kauppinen, A. Nuottajärvi, A. Obraztsov, Invited article: electric solar wind sail: toward test missions, Rev. Sci. Instrum. 81 (2010), https://doi.org/10.1063/1.3514548.
[58] Y. Leblanc, G.A. Dulk, J.-L. Bougeret, Tracing the electron density from the corona to 1 au, Sol. Phys. 183 (1) (1998) 165–180, https://doi.org/10.1023/A:1005049730506.
[59] E.C. Sittler Jr., J.D. Scudder, An empirical polytrope law for solar wind thermal electrons between 0.45 and 4.76 AU: Voyager 2 and Mariner 10, J. Geophys. Res. 85 (A10) (1980) 5131–5137, https://doi.org/10.1029/JA085iA10p05131.
[60] L. Gallana, F. Fraternale, M. Iovieno, S.M. Fosson, E. Magli, M. Opher, J.D. Richardson, D. Tordella, Voyager 2 solar plasma and magnetic field spectral analysis for intermediate data sparsity, J. Geophys. Res. Space Phys. 121 (5) (2016) 3905–3919, https://doi.org/10.1002/2015JA021830.
[61] J. Phillips, S. Bame, A. Barnes, B. Barraclough, W. Feldman, B. Goldstein, J. Gosling, G. Hoogeveen, D. McComas, M. Neugebauer, S. Suess, Ulysses solar wind plasma observations from pole to pole, Geophys. Res. Lett. 22 (23) (1995) 3301–3304, https://doi.org/10.1029/95GL03094.
[62] E.C. Stone, A. Frandsen, R. Mewaldt, E. Christian, D. Margolies, J. Ormes, F. Snow, The advanced composition explorer, Space Sci. Rev. 86 (1998) 1–22, https://doi.org/10.1023/A:1005082526237.
[63] L. Niccolai, A. Anderlini, G. Mengali, A.A. Quarta, Electric sail displaced orbit control with solar wind uncertainties, Acta Astronaut. 162 (2019) 563–573, https://doi.org/10.1016/j.actaastro.2019.06.037.
[64] L. Niccolai, A.A. Quarta, G. Mengali, Electric sail-based displaced orbits with a refined thrust model, Proc. Inst. Mech. Eng., G J. Aerosp. Eng. 232 (3) (2018) 423–432, https://doi.org/10.1177/0954410016679195.
[65] D. Odstrcil, P. Riley, X.P. Zhao, Numerical simulation of the 12 may 1997 interplanetary cme event, J. Geophys. Res. Space Phys. 109 (A2) (2004), https://doi.org/10.1029/2003JA010135.
[66] J. Hinterreiter, J. Magdalenic, M. Temmer, C. Verbeke, I.C. Jebaraj, E. Samara, E. Asvestari, S. Poedts, J. Pomoell, E. Kilpua, L. Rodriguez, C. Scolini, A. Isavnin, Assessing the performance of euhforia modeling the background solar wind, Sol. Phys. 294 (12) (2019), https://doi.org/10.1007/s11207-019-1558-8.
[67] C. Du, Z.H. Zhu, C. Wang, A. Li, T. Li, Equilibrium state of axially symmetric electric solar wind sail at arbitrary sail angles, Chin. J. Aeronaut. (2024), https://doi.org/10.1016/j.cja.2024.06.014.
[68] G.J. Bastos, R. Seifried, O. Brüls, Inverse dynamics of serial and parallel underactuated multibody systems using a dae optimal control approach, Multibody Syst. Dyn. 30 (2013) 359–376, https://doi.org/10.1007/s11044-013-9361-z.
[69] R. Bellman, Dynamic Programming, Reprint of the Sixth (1972) Edition, Dover Publications, Mineola, NY, 2003.
[70] V.L. Bakke, A maximum principle for an optimal control problem with integral constraints, J. Optim. Theory Appl. 13 (1974) 32–55, https://doi.org/10.1007/BF00935608.
[71] J.T. Betts, Practical Methods for Optimal Control and Estimation Using Nonlinear Programming, second edition, Society for Industrial and Applied Mathematics, Philadelphia, 2010.
[72] M. Diehl, H. Bock, H. Diedam, P.-B. Wieber, Fast Direct Multiple Shooting Algorithms for Optimal Robot Control, Springer Berlin Heidelberg, Berlin, Heidelberg, 2006, pp. 65–93.
[73] E.F. Camacho, C. Bordons (Eds.), Model Predictive Control, Springer-Verlag, Berlin, Heidelberg, 1999.
[74] Space Weather Prediction Center. National Oceanic and Atmospheric Administration, WSA-ENLIL Solar Wind Prediction, https://www.swpc.noaa.gov/products/wsa-enlil-solar-wind-prediction, 2024. (Accessed 23 April 2024).
[75] R. Waltz, J. Morales, J. Nocedal, D. Orban, An interior algorithm for nonlinear optimization that combines line search and trust region steps, Math. Program. 107 (3) (2006) 391–408, https://doi.org/10.1007/s10107-004-0560-5.